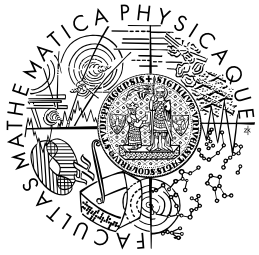

FACULTY
OF MATHEMATICS
AND PHYSICS
Charles University

BACHELOR THESIS

Iveta Zatočilová

Study of Radiation Damage in Silicon Strip Detector for ATLAS ITk

Institute of Particle and Nuclear Physics

Supervisor of the bachelor thesis:	Ing. Marcela Mikeštíková, Ph.D.
Study programme:	Physics
Study branch:	General Physics

Prague 2019

I declare that I carried out this bachelor thesis independently, and only with the cited sources, literature and other professional sources.

I understand that my work relates to the rights and obligations under the Act No. 121/2000 Sb., the Copyright Act, as amended, in particular the fact that the Charles University has the right to conclude a license agreement on the use of this work as a school work pursuant to Section 60 subsection 1 of the Copyright Act.

In ..... date ..... signature of the author

On this place, I would like to firstly and most importantly thank my supervisor Ing. Marcela Mikeštíková, Ph.D. for her patience, inspiring guidance and supportiveness, valuable advice during the measurements and evaluation of the results. I greatly thank to RNDr. Jiří Kroll, Ph.D. for wire bonding the sensors and in particular for his thorough reviews on the thesis.

Secondly, I would like to thank Doc. RNDr. Zdeněk Doležal, Dr. for introducing me to the topic of particle detectors and also for introducing me to my supervisor and research group at Institute of Physics of the Czech Academy of Sciences.

Last but not least I must thank to my parents and my wonderful best friend.

Title: Study of Radiation Damage in Silicon Strip Detector for ATLAS ITk

Author: Iveta Zatočilová

Institute: Institute of Particle and Nuclear Physics

Supervisor: Ing. Marcela Mikeštíková, Ph.D., Institute of Physics of the Czech Academy of Sciences

Advisors: RNDr. Jiří Kroll, Ph.D., doc. RNDr. Zdeněk Doležal, Dr.

Abstract: Ionizing radiation causes bulk and surface damages in silicon detectors. The significant bulk damage is caused also by neutrons. Those damages influence the detection performance of silicon strip detectors. The main purpose of this thesis is to study the effects of radiation damage in silicon strip sensors by performing electrical tests on them. Tested silicon strip sensors were designed for the replacement of the current Inner Detector of the ATLAS experiment by a new all-silicon Inner Tracker. This replacement is needed because of the upgrade of the Large Hadron Collider (LHC) into the High-Luminosity LHC.

Keywords: Silicon strip detector, Radiation damage, ATLAS ITk Upgrade, Detection performance, Electrical parameters

Contents

Introduction

The main goal of the ATLAS experiment is to verify the results of the standard model of elementary particles and their interactions. It should also provide important information on the origin and evolution of the universe, composition and properties of the dark matter, etc. The biggest achievement of the ATLAS detector is discovery of the Higgs boson, announced in 2012 [1]. To be able to study production of the Higgs boson and its individual decays with much higher statistics, it is necessary to upgrade the current LHC accelerator to the High-Luminosity LHC (HL-LHC). This upgrade is also critical for searching for the extremely rare processes potentially sitting beyond the standard model.

During the Long Technical Shutdown 3, planned between 2024 - 2026, the LHC accelerator will be upgraded into the HL-LHC, which will increase the luminosity from the current $2 \cdot 10^{34}$ cm^{-2}s^{-1} to the new maximal value of $7.5 \cdot 10^{34}$ cm^{-2}s^{-1}. The increased luminosity will lead to higher radiation levels in the ATLAS experiment. The current Inner Detector of the ATLAS experiment was not designed for newly created radiation environment and it will not be able to preserve its detection performance under the resulting conditions. Therefore, the upgrade of LHC requires complete replacement of the ATLAS Inner Detector by a new all-silicon Inner Tracker (ITk).

The ATLAS ITk detector will be build from radiation hard components, which should be able to withstand the radiation damage corresponding to the total integrated luminosity of 4000 fb^{-1}. As the average number of the hard p-p interactions per bunch crossing will increase by factor of 10, the ITk detector needs to have ten times more readout channels than the current Inner Detector to keep the same level of detector occupancy and to avoid the data bandwidth saturation. The ITk will be newly also a part of the hardware trigger as the tracking information will be added to trigger objects provided by calorimeters and muon system. The trigger threshold will be lowered which directly benefits the physics performance.

The new Inner Tracker will be operational for more than 10 years, during which ATLAS aims to accumulate a total data set of 4000 fb^{-1}. This goal presents a challenge for the design of an all-new tracking system that consists of a pixel detector at small radius close to the beam line surrounded by a large-area strip tracking detector. The basic component of the ITk strip detector will be radiation hard silicon micro-strip sensors with n$^+$-implants in p-type bulk (n$^+$-in-p). The n$^+$-in-p detectors will replace detectors with p$^+$-implants in n-type bulk (p$^+$-in-n) that are used in Semiconductor Tracker (SCT) of the current Inner Detector. The whole replacement of Inner Detector by the new Inner Tracker is coordinated by ATLAS ITk Collaboration.

This thesis studies the effects of gamma irradiation on the electrical characteristics of n$^+$-in-p strip sensors. The tests were performed on the ATLAS17LS strip sensors, manufactured by Hamamatsu Photonics (HPK), in the clean laboratory installed at The Institute of Physics of the Czech Academy of Sciences (IoP CAS).

The thesis is divided into five chapters. The first chapter describes the interactions of particles with matter. The second chapter provides the introduction

to semiconductor particle detectors. It describes the principles of detection of different particles in semiconductor detectors. The third chapter is dedicated to radiation effects in semiconductor detectors. The LHC accelerator, its experiment ATLAS and the replacement of ATLAS Inner Detector by the new Inner Tracker are described in the chapter number 4. Finally, the own results of measurements of electrical characteristics of ATLAS17LS sensors are described in detail in chapter 5.

1. Interaction of Particles with Matter

To understand the principles of detection of electrically-charged particles in silicon detector, we have to get to know the basics of the particle interaction mechanisms with the matter. Due to the interaction of particles with matter, we are able to detect these particles. However, the interaction that provides the possibility of detecting the particles may also cause radiation damage to the detector.

1.1 Interaction of Charged Particles with Matter

When the charged particle passes through the matter it can interact with atomic electrons or with the nucleus.

In the interaction with atomic electrons the charged particle collides inelastically losing its energy and the incident atom suffers excitation or ionization. When the charged particle interacts with the nucleus, the incident particle is deflected by the electric field of this nucleus undergoing elastic interactions or the particle can be accelerated and radiates Bremsstrahlung photons. Both processes lead to the particle energy loss.

Energy loss of a heavy charged particles through inelastic collisions can be calculated by Bethe-Bloch formula [2]

$$-\frac{dE}{dx} = 4\pi N_{\mathrm{A}} r_{\mathrm{e}}^2 m_{\mathrm{e}} c^2 \frac{Z}{A}\frac{z^2}{\beta^2}\Big[\ln\Big(\frac{2m_{\mathrm{e}}\gamma^2 c^2\beta^2}{I}\Big) - \beta^2 - \frac{\delta}{2}\Big], \tag{1.1}$$

where N_{A} stands for Avogadro number, r_{e} is for classical electron radius, m_{e} is the electron mass, Z is the medium atomic number and A is the mass atomic number of the absorber, z is the incident particle charge, β is the incident particle velocity, γ is the Lorentz factor, I is the average ionization energy and δ stands for density correction factor.

The incident particle energy loss calculated by Bethe-Bloch formula depends on the incident particle velocity.

The minimal energy loss occurs when $\beta\gamma \approx 3.5$ [3].

1.2 Interaction of Photons

Photons interact with matter, while producing charged particles, predominantly through the following processes – Photoelectric process, Compton scattering and Pair production. The dependence of the photon contribution of the individual processes on energy is shown in Fig. 1.1.

- Photoelectric process: $\gamma + \text{atom} \rightarrow \text{atom}^+ + e^-$,
- Compton scattering: $\gamma + e^- \rightarrow \gamma + e^-$,
- Pair production: $\gamma + \text{nucleus} \rightarrow e^+ + e^- + \text{nucleus}$.

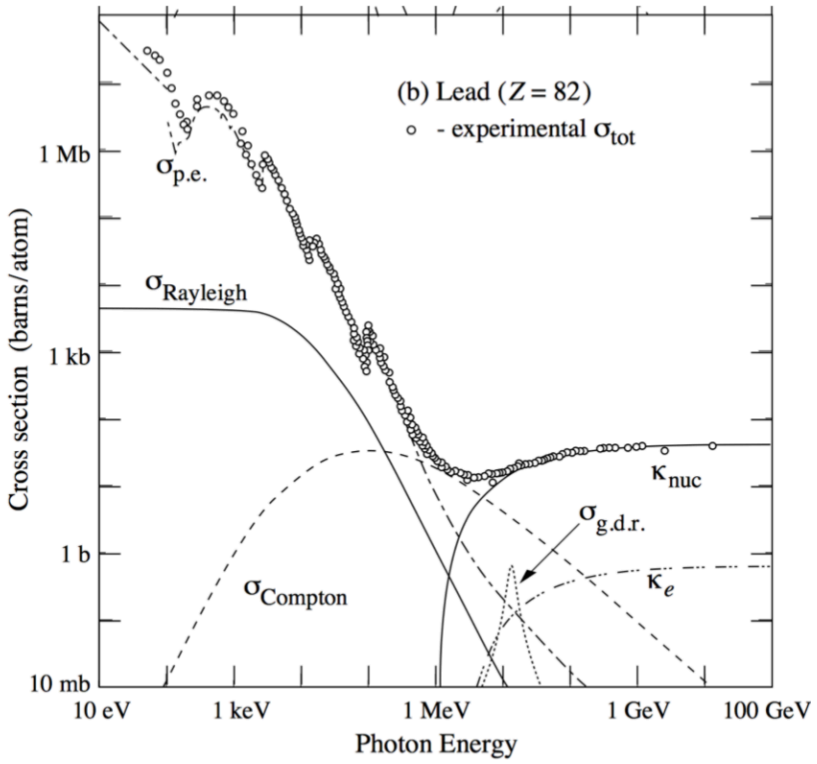

Figure 1.1: Dependence of the photon contribution of individual processes on energy [2].

Photoelectric process or photo-effect is a process of photon absorption leading to ionization of an atom and emission of electron with kinetic energy T_e, where $T_\mathrm{e} = E_0 - I_\mathrm{i}$, I_i is the binding energy of the electron and E_0 is the energy of photon. This interaction process dominates for photons with $E_0 < 0.1$ MeV.

Compton scattering is the scattering of a photon by a charged particle. The predominant energy of photons participating in Compton scattering is $0.1 \text{ MeV} < E_0 < 10$ MeV. Compton scattering occurs when the incident high-energy photon is deflected from its original path by an interaction with an electron. The electron is ejected from its orbital position and the high-energy photon loses energy because of the interaction but continues to travel through the material along an altered path. The energy shift depends on the angle of scattering and not on the nature of the scattering medium. Since the scattered high-energy

photon has less energy, it has a longer wavelength than the incident photon. The difference between the initial and final wavelength of the interacting photon can be described as

$$\lambda_{\mathrm{f}} - \lambda_{\mathrm{i}} = \frac{h}{m_{\mathrm{e}}c}(1 - \cos\phi), \tag{1.2}$$

where λ_{i} stands for the initial wavelength of the photon, λ_{f} is for the final wavelength of the scattered photon, h is the Planck constant, m_{e} is the invariant mass of the electron involved in the interaction, c is the speed of light and ϕ stands for the angle of the scattering.

Pair production is the creation of an electron-positron pair from high-energy photon in the electromagnetic field of nucleus. The creation is possible only if the energy of photon E_0 is higher than $2E$, where E is rest mass of electron $E = 511$ keV.

1.3 Cobalt-60 radioactive source

The radioactive isotope ^{60}Co was used for irradiation of our sensors. The isotope ^{60}Co decays to the excited state of ^{60}Ni by beta decay emission of an electron with the energy of 0.31 MeV. Excited ^{60}Ni then decays to the ground state by emitting gamma rays with energies 1.17 MeV and 1.33 MeV, see Fig. 1.2. This decay path is followed 99.88 % of the time.

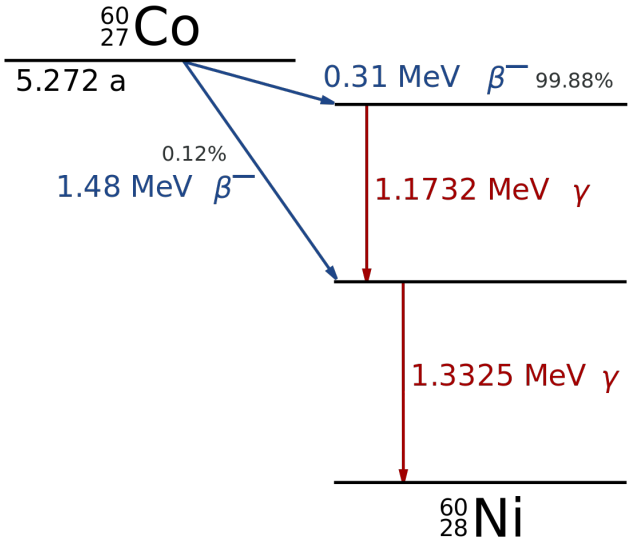

Figure 1.2: Decay scheme of Cobalt-60 [4].

Photons with the energy of ∼1 MeV created during the decay of the ^{60}Co source interact with the silicon bulk predominantly by the Compton scattering.

2. Introduction to Semiconductor Particle Detectors

This chapter deals with semiconductors and their use as particle detectors. Compared to gas detectors, semiconductor detectors have a high density, therefore the particle loses a large amount of energy on a short distance. The diffusion effect is also smaller compared to the gas detectors, so the spatial resolution is significantly better than in the gas detectors. The ionization energy needed to the creation of electron-hole pair in silicon is just a few eV in comparison to the gas detectors where it is approximately 30 eV. The average energy for creation of e-h pair in silicon is 3.6 eV.

2.1 Properties of Semiconductors

Semiconductors are solid crystals usually Si or Ge of the Fourth group of the periodic table or compounds such as GaAs. The electrical conductivity value of semiconductors is higher than insulators but lower than conductors. The conduction band of semiconductors is separated from valence band by the energy gap which is approximately 1 eV wide. Because of the thin energy gap electrons from valence band can be thermally excited into the conduction band while leaving the hole in the valence band. This hole can be filled by the neighbouring electron and by repeating this process electrons are moving in the conduction band and holes are moving in the valence band through the crystal in opposite directions. It is how the semiconductors conduct current.

Intrinsic semiconductors are semiconductors that contain no impurities compared with the number of thermally generated electrons and holes. Intrinsic semiconductors are rarely used in semiconductor devices since it is extremely difficult to obtain sufficient purity in the material.

Extrinsic semiconductors are semiconductors made by adding small fractions of specific impurities into the crystal. It can be performed either during crystal growth or later in selected regions of the crystal. The process is called doping. Depending on the type of added material, n-type semiconductors have an excess of electrons in the conduction band while p-type semiconductors have additional holes in the valence band [5]. The schematic representation of the energy band of semiconductors is shown in Fig. 2.1.

By doping, adding the impurities into the crystal, we can control the conductivity of semiconductors. The required concentrations of added material are 10^{12} – 10^{18} cm^{-3}. Typical concentration of dopant is 10^{12} cm^{-3} for radiation detectors.

2.2 P-N Junction as a Detector

P-N junction is obtained by joining extrinsic semiconductors of opposite doping together. The p- and n- regions are initially electrically neutral, but thanks to the thermal diffusion electrons and holes are driven across the junction and also cre-

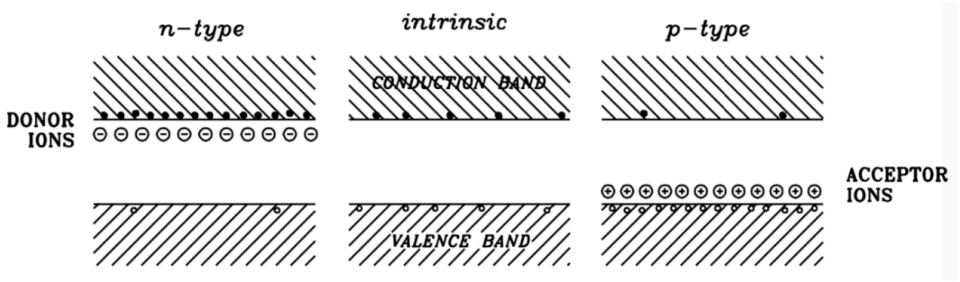

Figure 2.1: Schematic energy band representation of semiconductors [5].

ates a region free of mobile carries called the depletion region. Diffused electrons from n-region to p-region leave a net positive charge in the n-region. Their diffusion into p-region builds up a potential V_{bias} between p- and n-regions as shown in Fig. 2.2.

If we apply forward bias voltage, the p-type is connected with the positive terminal and the n-type is connected with the negative terminal, on the p-n junction the potential difference between p- and n- regions decreases and the flow of electrons and holes across the junction is supported. Reverse bias voltage, the p-type is connected with the negative terminal and the n-type is connected with the positive terminal, raises the potential barrier. It reduces the concentration of electrons and holes at the junction and widens the depleted region [5].

The depleted region of p-n junction is the region sensitive to the external radiation. As the applied reverse bias widens the depleted region of the junction, the reverse biased p-n junctions are used as detectors.

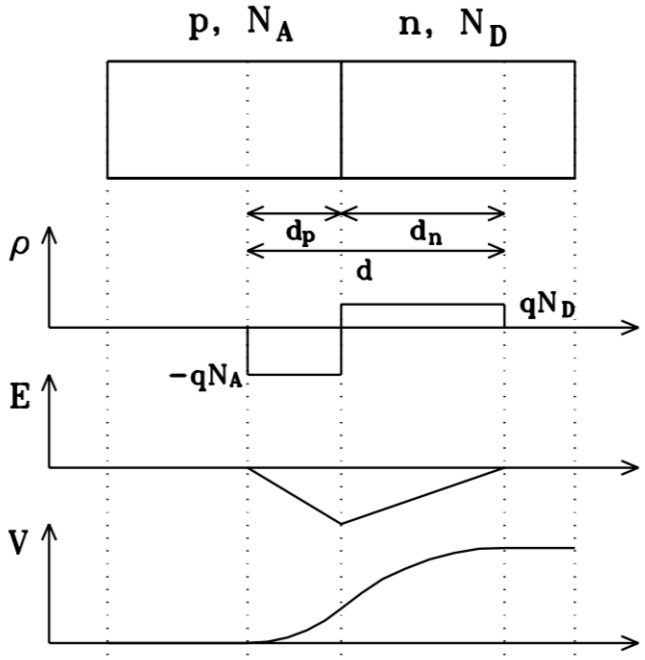

Figure 2.2: Charge carrier density ρ, electric field E and electric potential V in the depleted region. N_{A} and N_{D} stands for acceptor and donor concentrations [5].

The width of the depleted region w_{d} can be determined using the equation

$$w_{\mathrm{d}} = \sqrt{2\epsilon_0 \epsilon_{\mathrm{Si}} \rho \mu_{\mathrm{e}} (V_{\mathrm{bias}} + V_{\mathrm{R}})}, \tag{2.1}$$

where ϵ_0 is the vacuum permittivity, ϵ_{Si} the relative permittivity of silicon, ρ is the n-type silicon resistivity, μ_{e} the electron mobility, V_{bias} is built-in potential between the p- and n-region and V_{R} is negative reverse applied voltage [5].

A p-n junction with applied external voltage yields a capacitance. The total capacitance is the sum of the diffusion capacitance, which dominates in strongly forward-biased junctions, and the junction capacitance dominating for reverse-biased junctions and their depleted regions. The capacitance depends on the dielectric constant, the area of the depleted region S, carrier concentration N and applied voltage V

$$C \cong S\Big(\frac{e\epsilon_{\mathrm{Si}}\epsilon_0 N}{2V}\Big)^{1/2}, \tag{2.2}$$

where e is elementary charge.

The junction capacitance of depleted region is calculated using the expression for the parallel plate capacitor

$$C = \epsilon\frac{A}{w_{\mathrm{d}}} = \left\{ \begin{array}{ll} A\sqrt{\frac{\epsilon_0\epsilon_{\mathrm{Si}}}{2\rho\mu_{\mathrm{e}}V_{\mathrm{R}}}}, & \text{for } V_{\mathrm{R}} < V_{\mathrm{FD}} \\ A\frac{\epsilon_0\epsilon_{\mathrm{Si}}}{d} = \text{const}, & \text{for } V_{\mathrm{R}} \geq V_{\mathrm{FD}} \end{array} \right\}, \tag{2.3}$$

where A is the area of the depleted region and d is the detector's width. As mentioned the sensitive volume of detector is equal to the area of the depleted region. If we set the width of the depleted region w_{d} as the width of the detector d, we can get the equation for the calculation of the full depletion voltage

$$V_{\mathrm{FD}} = \frac{d^2}{2\epsilon_{\mathrm{r}}\epsilon_0\rho\mu_{\mathrm{e}}}. \tag{2.4}$$

If the applied voltage is lower than the full depletion voltage, the detector is under-depleted with inactive volume. By applying higher voltage than V_{FD}, we get over-depleted detector. If the applied voltage is too high, the detector may be destroyed by electric field break-downs. The ideal operational voltage for the detector is voltage higher than full depletion voltage, but not too high to prevent the detector from break-downs [5].

The current of reverse biased diode is called leakage or reverse current.
The leakage current depends on the width of the depleted region and the temperature at which it is measured. It has three main sources [6], [7].

1. Thermally generated electron-hole pairs originating from the recombination and trapping centers in the depletion region. Due to the applied external electric field, they could not recombine and drift across the crystal to the electrodes. Moving charge results in a current.

2. The reverse current, which is formed by the movement of minority charge carriers, that migrate to the opposite sides of the p-n junction due to the applied external voltage.

3. The interface between silicon and SiO_2 layer has a high density of defects which act as charge carrier generation centres. Generated carriers drift along the electric field and are responsible for the surface part of the reverse current.

2.3 Principles of Particle Detection in Semiconductor Detectors

Semiconductor detector is a reversed-biased diode. The charged particle passing through the depleted zone of the detector is loosing its energy by excitation or ionization of the silicon atoms. The electron-hole pairs produced along its way are carried out by the electric field to the individual electrodes of the detector and collected. The energy deposited in the detector material by ionizing particle is then converted into the current pulse corresponding to the total value of ionization energy collected in the detector.

2.4 Position Sensitive Semiconductor Detectors

Position sensitive detectors can be obtained by dividing one side of p-n junction into segments with each segment representing an electrode with a separate readout. Electrodes could be made in a form of strips or pads. In a strip detector every strip represents a p-n diode. We distinguish two types of position sensitive semiconductor detectors - detectors with p^+ implants in n^- type bulk and detectors with n^+ implants in p^- type bulk.

The detector is biased by reversed bias voltage. The electrons produced by ionizing particle, that crosses the depleted region of the diode, are in p^+-in-n detector drifted to the back-plane of detector, while the holes are drifted to the p^+ implants. The charge collected in the p^+ implants is induced to the aluminum strips.

On the other hand, the n^+-in-p type detector has p^- bulk with n^+ implants. The electrons are drifted to the n^+ implants and the holes are drifted to the back-plane of detector. Fig. 2.3 shows the schematic cross-section of n^+-in-p silicon strip detector with n^+ implants and p^- bulk.

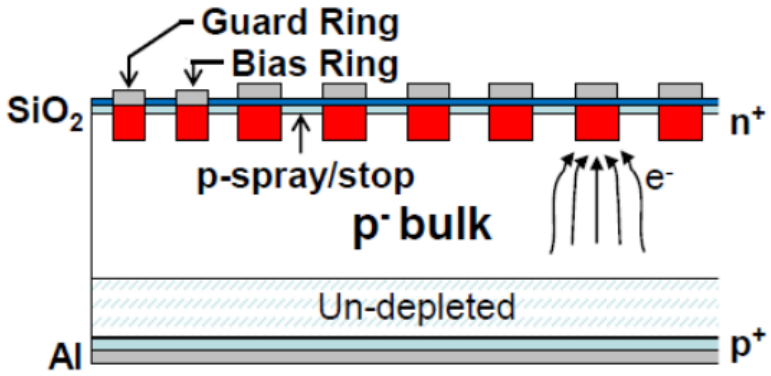

Figure 2.3: Schematic cross-section of n^+-in-p silicon strip detector [8]

Layout of ATLAS17LS silicon strip sensor is shown in Fig. 2.4. The sensor has a typical layout of n^+-in-p silicon strip sensor type. Besides of the aluminium readout strips, that include AC and DC contact pads, we can also see polysilicon bias resistors and a bias ring and an outer guard ring along the whole sensor. Every n^+ implant strip is capacitively coupled through a thin dielectric layer made of SiO_2 to a metal readout strip and connected to a polysilicon bias resistor, see Fig. 2.5. The polysilicon bias resistors are connected to the bias ring that keeps all the strips on the same potential. The outer guard ring shapes the electric field inside the sensitive area of the sensor and leads away the leakage currents from the edges, therefore ensures the high voltage stability [9]. All the strips are isolated using p-stop implants or p-spray technology. The front side of the sensor is passivated by a thin layer of SiO_2 and the back side of the sensor is covered by uniform metallisation. The physical thickness of the sensors is 300 - 320 μm, while the active thickness is $\geq$ 90 % [10].

In Fig. 2.4, there are also visible AC and DC pads and a bias pad. The contact pads are able to withstand probing with standard probe needles during the test measurements and they are also compatible with standard ultrasonic aluminium wire bonding technology that will be used for the connection to readout electronics. The readout electronics of a detector consists of chips with an implemented set of preamplifiers and a circuit determined to send signals to be read out.

The effective detection performance is provided for the voltages greater than the full depletion voltage applied between the back-plane and the implants of a detector. The position of the incident particle is determined by the strip that is showing the signal. The precision of the detection performed by the detector depends on the distance between the strips, parameter of the readout electronics, and on the chosen readout method.

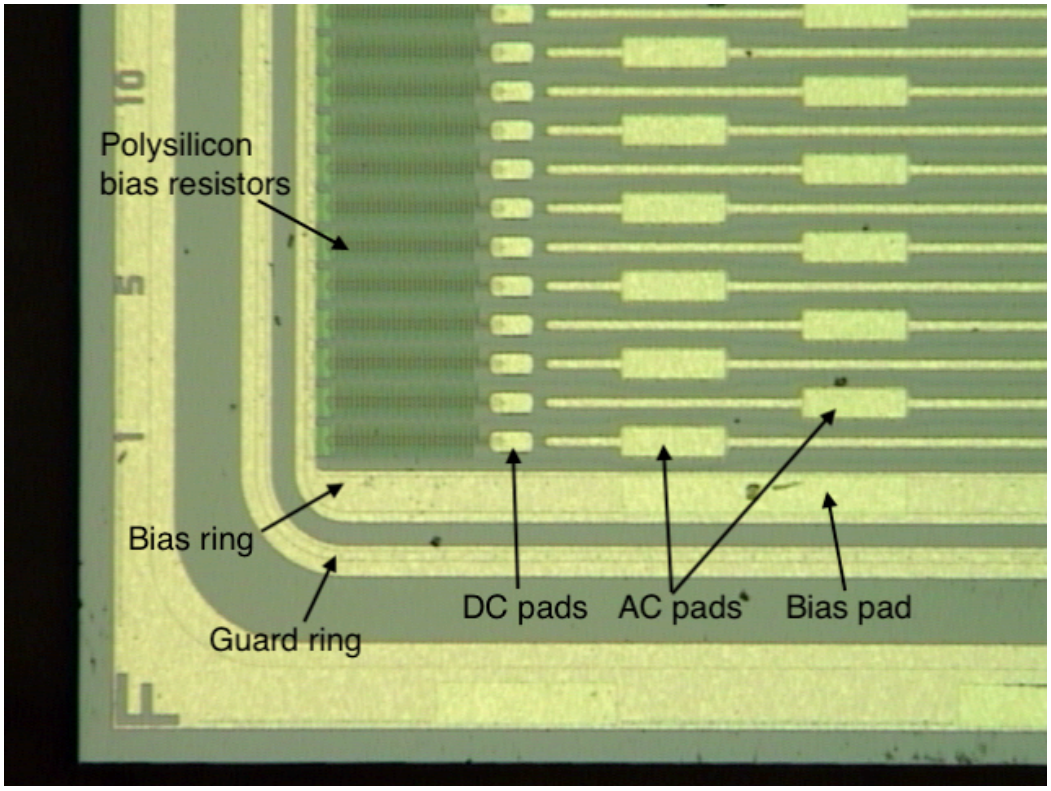

Figure 2.4: Sensor layout of ATLAS17LS.

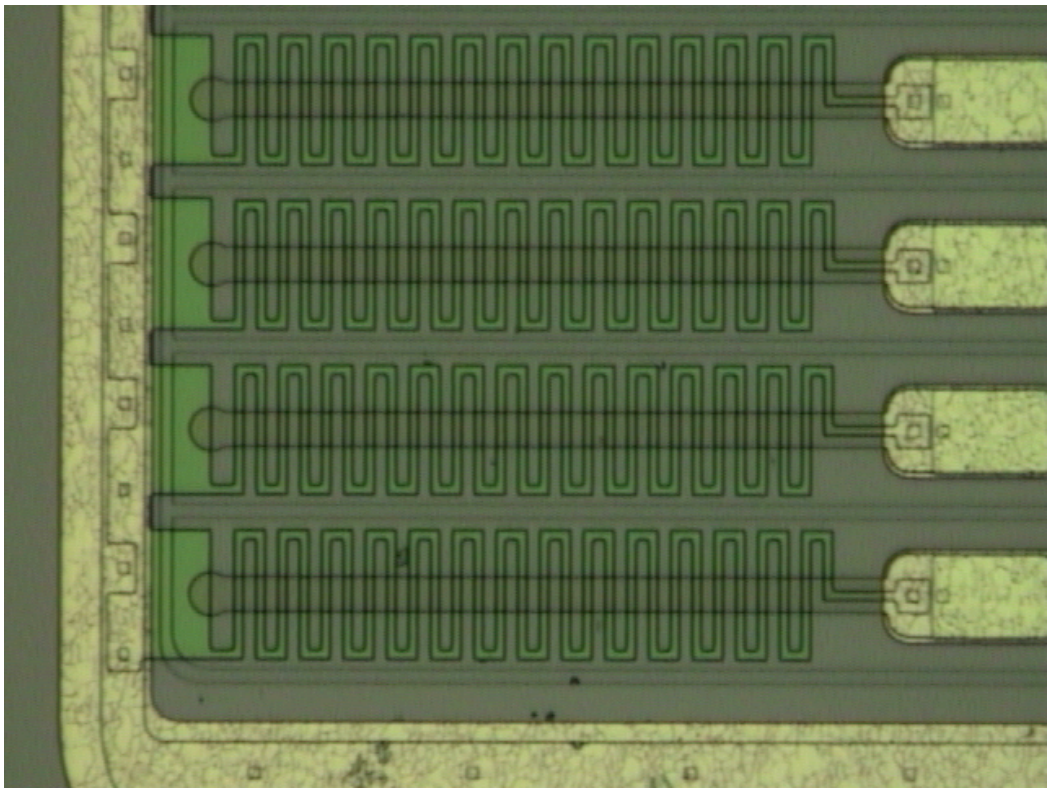

Figure 2.5: Closeup image of polysilicon bias resistor of ATLAS17LS sensor.

3. Radiation Effects in Semiconductor Detectors

The radiation impacts detection performance of silicon detectors. The silicon detectors in ATLAS ITk will be exposed to high radiation levels for several years and their detection performance will deteriorate. The damage mechanisms in silicon detectors can be divided into two main classes – bulk and surface damage.

3.1 Bulk Damage

Bulk damage to the detector is caused by incident particles colliding with lattice silicon atoms. The displacement damage depends on the energy of a colliding particle and momentum transfer to the lattice atoms [11]. The particles of energy ∼25 eV cause the damage by displacing a Primary Knock on Atom (PKA) out of its lattice site. It leads to the creation of point defects such as vacancies and interstitials.

The vacancies and interstitials can move at temperatures higher than 150 K. Some of the defects are able to interact together and form a complex of point defects which is stable at room temperature. Some of the defects can also annihilate or diffuse out of the structure leaving the semiconductor undamaged. Some of the defects can annihilate, when a vacancy is filled in with an interstitial, leaving the semiconductor undamaged. The resulting damage is formed by stable defects. For recoil energies above 5 keV there is a large cluster formed at the end of the primary PKA track [12].

The resulting damage is measured in NIEL (Non-Ionizing Energy Loss), see Fig. 3.1, that is the sum of the whole energy of the incident particle that is used for the displacement and is compared with damage caused by 1 MeV neutrons with the same fluence [11].

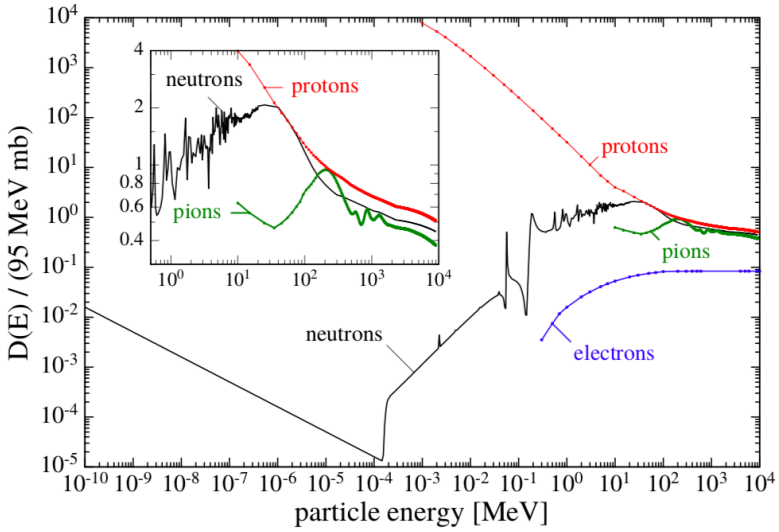

Figure 3.1: Non Ionizing Energy Loss NIEL for different particles [12].

3.2 Surface Damage

Surface damage is the damage caused by the radiation to the insulator layer of the detector. The insulator layer of ATLAS17LS sensors is made of SiO_2, see Fig. 3.1, which is a crystal with irregular structure that is not significantly affected by the displacement damages. Therefore, the main damage to the surface region is caused by the ionization. Charged particles while passing through the Si-bulk and the SiO_2 layer create electron-hole pairs. Due to very different mobility of electrons and holes most of the free electrons leave the SiO_2, whereas holes get trapped in the SiO_2. It leads to the formation of a positive oxide charge layer. The accumulation of positive charge attracts the negative charge from the bulk of the detector and the conductive electron channels are created.

The surface damage is considered as the main source of the increased surface leakage current, that may cause early break-down voltages, decreased interstrip resistance, etc. [13].

3.3 Radiation Damage in Sensor

As already mentioned above the sensors exposed to radiation show deterioration in their detection performance that results in changes in electrical parameters of the sensors.

3.3.1 Leakage current after irradiation

The leakage current of an irradiated sensor depends linearly on the fluence of exposure ϕ by equation

$$\frac{\Delta I}{V} = \alpha\phi. \tag{3.1}$$

The numerical value of the parameter α was determined as $\alpha \approx 4 \cdot 10^{-17}$ cm^{-1} for sensors measured at 20 °C that had been annealed for 80 minutes at the temperature of 60 °C and its value does not depend on the silicon type and its resistivity [7].

Leakage current of semiconductors depends on temperature T at which it is measured. We can use following parametrization for silicon particle detectors

$$I(T) \propto T^2 \exp\left(\frac{-E_{\text{eff}}}{2k_{\text{B}}T}\right), \tag{3.2}$$

where $E_{\text{eff}} \approx 1.2$ eV, k_{B} is the Boltzmann constant. The dependence of leakage current on the fluence for different silicon sensors is shown in Fig. 3.2. The leakage current can be decreased by performing the measurement at decreased temperature [14].

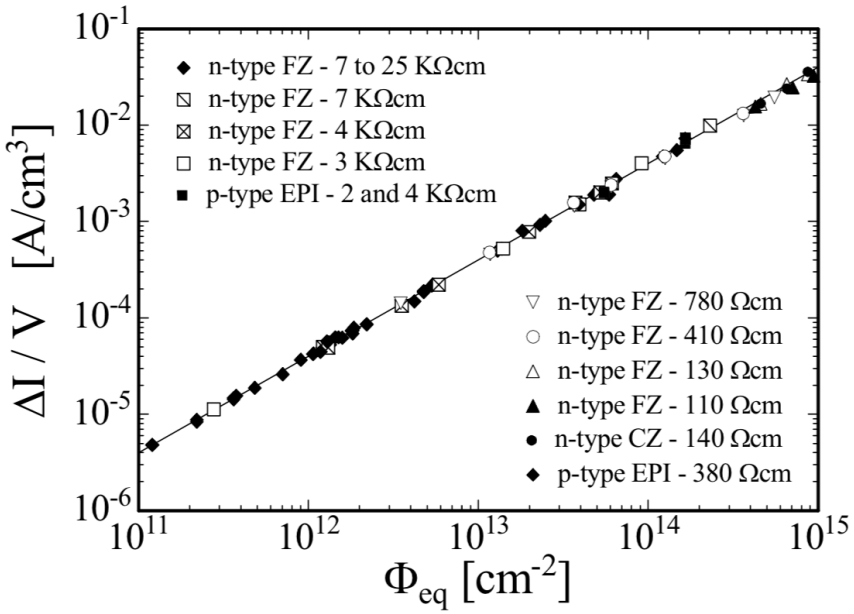

Figure 3.2: Dependence of the leakage current on fluence for different silicon sensors measured after annealing for 80 minutes at the temperature of 60 °C [12].

3.3.2 Full depletion voltage after irradiation

When the holes or electrons are trapped by a complex of defects, their original charge can be changed or they can even lose their function of donors or acceptors.

The radiation-induced defects lead to a change in the effective space charge $q|N_{\text{eff}}|$ that is reflected in a change of the depletion voltage V_{dep} of silicon sensors. The depletion voltage V_{dep} is given as

$$V_{\text{dep}} = \frac{q|N_{\text{eff}}|d^2}{2\epsilon\epsilon_0}, \tag{3.3}$$

where d is the thickness of the device, q is the elementary charge, ϵ is the relative permittivity of silicon and ϵ_0 is the vacuum permittivity.

Fig. 3.3 shows the evolution of the depletion voltage for an n-type sensor with particle fluence. Irradiation of the sensor results in the formation of negative space charge which compensates the initial positive space charge. With increasing particle fluence, the net space charge decreases and reaches very low values corresponding to almost intrinsic silicon. This point is called type inversion as the space charge sign changes from positive to negative. Increasing the particle fluence beyond the point of type inversion leads to more and more negative space charge values. The depletion voltage rises accordingly and eventually reaches values that cannot be applied to the detector any more without causing breakdown. The applied voltage will have to be kept below the depletion voltage and the detector is operated underdepleted. For high-resistivity p-type sensors, no type inversion is usually observed as the initial space charge is already negative before irradiation [14].

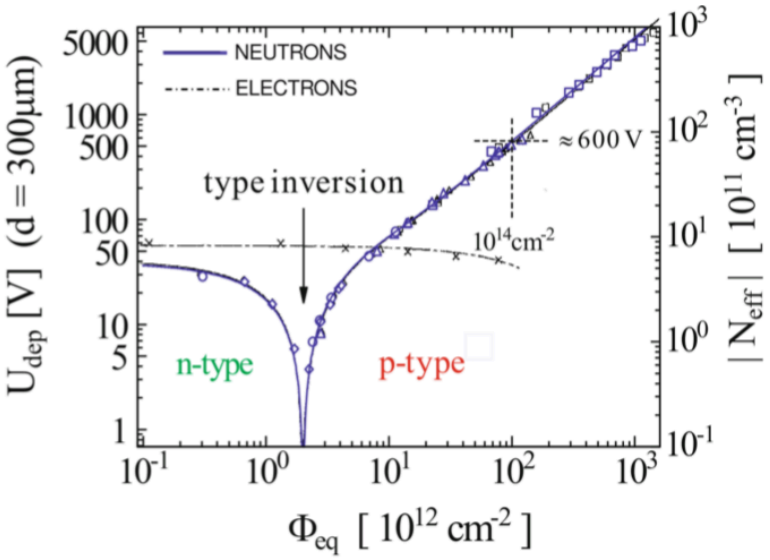

Figure 3.3: Dependence of the full depletion voltage and the effective doping concentration of an originally n-typed silicon sensor on the total delivered fluence of neutrons and electrons is shown in units of 1 MeV·n_{eq}·cm^{-}2 [14].

3.4 Annealing

Annealing is the effect of healing the damage caused to the crystal by radiation thanks to the temperature at which the sensor is kept. The primary defects are mobile at room temperature, the secondary defects may become mobile at higher temperatures. Therefore by keeping the sensor at higher temperatures for defined time the radiation-generated damage may partially disappear.

The process is not perfect, but the detection performance of the sensor improves after annealing as we can see by comparing its electrical parameters before and after annealing. The effect of the annealing on the effective space charge can be described by the equation

$$\Delta N_{\mathrm{eff}}(\Phi_{\mathrm{eq}}, t(T_{\mathrm{a}})) = N_{\mathrm{eff},0} - N_{\mathrm{eff}}(\Phi_{\mathrm{eq}}, t(T_{\mathrm{a}})), \tag{3.4}$$

$$\Delta N_{\mathrm{eff}}(\Phi_{\mathrm{eq}}, t(T_{\mathrm{a}})) = N_{\mathrm{A}}(\Phi_{\mathrm{eq}}, t(T_{\mathrm{a}})) + N_{\mathrm{C}}(\Phi_{\mathrm{eq}}) + N_{\mathrm{Y}}(\Phi_{\mathrm{eq}}, t(T_{\mathrm{a}})), \tag{3.5}$$

where $N_{\mathrm{eff},0}$ represents the initial value of the effective space charge before irradiation and ΔN_{eff} is a function of total delivered fluence and time. The time dependence is in itself subject to the annealing temperature T_{a}. As indicated in Fig. 3.4 and obvious from equation 3.5 ΔN_{eff} consists of three components: a short term beneficial annealing N_{A}, a stable damage part N_{C} and the reverse annealing component N_{Y}. The stable damage part can be expressed by

$$N_{\mathrm{C}}(\Phi_{\mathrm{eq}}) = N_{\mathrm{C0}}(1 - \exp(-c\Phi_{\mathrm{eq}})) + g_{\mathrm{C}}\Phi_{\mathrm{eq}}, \tag{3.6}$$

where N_{C} is depending exponentially on the fluence, with a final value N_{C0}, and a fluence proportional introduction of stable acceptors, with an introduction rate g_{C} [15].

Fig. 3.4 shows the dependence of ΔN_{eff} on the annealing time. The short term beneficial annealing amplitude is given by $N_{\text{A}} = g_{\text{A}}\Phi_{\text{eq}}$ and the reverse annealing amplitude is given by $N_{\text{Y}} = g_{\text{Y}}\Phi_{\text{eq}}$.

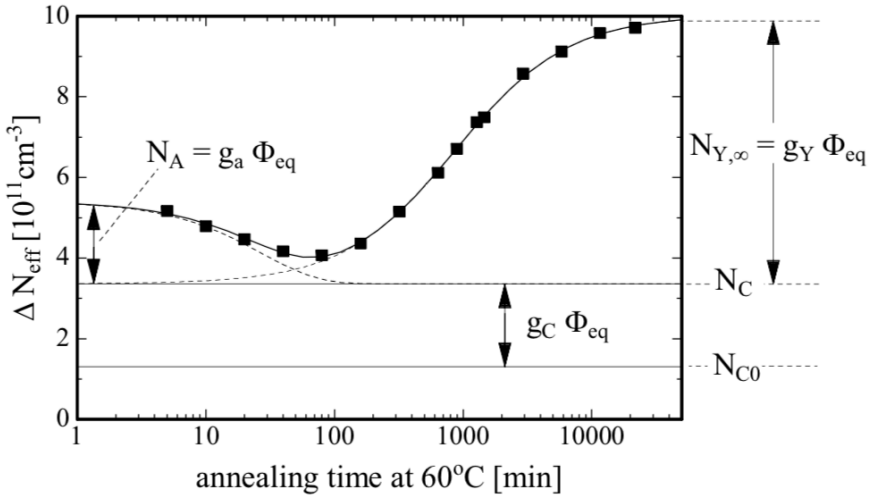

Figure 3.4: Annealing behaviour of the radiation induced change in the effective doping concentration ΔN_{eff} at 60 °C [15].

4. Strip Sensors for ITk ATLAS

CERN is the acronym for the European Center for Nuclear Research.
The acronym stands for the French name of the organization "Conseil Européen pour la Recherche Nucléaire". The laboratory was founded in 1954 and was primarily supposed to study atomic nuclei, later the high-energy physics became the main point of interest at CERN.

4.1 LHC and Its Experiments

The Large Hadron Collider is the particle accelerator situated at CERN near Geneva. The LHC consists of a 27 km long ring of superconducting magnets with a number of accelerating structures that boost the energy of the particles along the way placed 100 meters underground. The LHC is the most advanced facility in the world for the investigation of the structure of matter at its smallest scales. On its circumference LHC hosts seven experiments, detectors that analyse the myriad of particles produced by collisions of protons or lead nuclei in the accelerator. The biggest experiments are ATLAS, CMS, ALICE and LHCb.

We hope that LHC experiments will give us answers to questions such as the origin of mass, the nature of dark matter, new forces and particles or the nature of the quark-gluon plasma.

4.2 Experiment ATLAS

The ATLAS experiment is a general-purpose particle physics experiment run by an international collaboration. The experiment contains the largest volume detector which was ever constructed for a particle collider. The cylinder-shaped detector is 46 m long, it is 25 m in the diameter and it is located in a cavern 100 m below the ground. The detector itself consists of six different detecting subsystems that lie in the layers concentrically around the collision point. The detection layers altogether record the trajectory, momentum and energy of the particles created in the collisions of two countercurrent proton or heavy ion beams. The schematic layout of the ATLAS detector with its detection layers - the Pixel detector, Semiconductor tracker, Transition radiation tracker, Electromagnetic calorimeter, Hadronic calorimeter and Muon spectrometer is shown in Fig. 4.1.

The Pixel detector, Semiconductor tracker and Transition radiation tracker are the parts of the ATLAS Inner Detector (ID). The ID measures the trajectory, momentum and charge of electrically-charged particles produced in each proton-proton collision. The Electromagnetic and Hadronic calorimeters measure energy loss of passing particles. The Electromagnetic calorimeter is designed for measurements of energy loss of electrons and photons and the Hadronic calorimeter focuses on energy loss of hadrons. The Muon spectrometer identifies muons and measures their momenta.

Other important component of the ATLAS detector is the Magnet System, that enables measurements of particle momenta by bending the particle trajec-

tories in the ID and Muon Spectrometer.

Integrated with the detector components there is the Trigger and Data Acquisition System and the Computing System. The Trigger and Data Acquisition System is specialized multi-level computing system, which selects physics events with distinguishing characteristics. The Computing System develops and improves computing software used to store, process and analyse vast amounts of collision data at 130 computing centres worldwide [16].

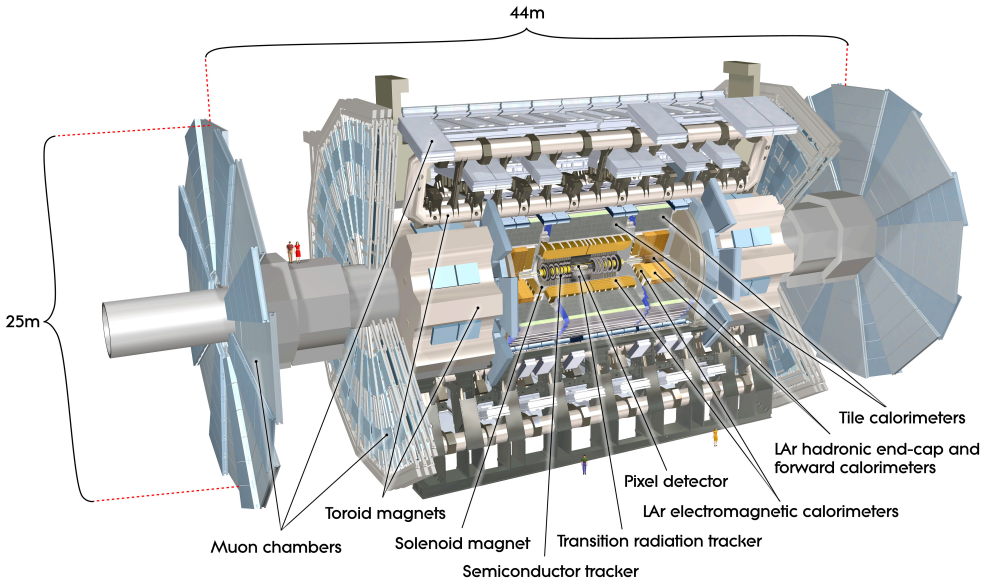

Figure 4.1: Computer generated image of the whole ATLAS detector [17].

4.3 ATLAS Phase II Upgrade

By the second half of 2026 the LHC will have upgraded into the High-Luminosity LHC and will have achieved an ultimate luminosity of $\mathcal{L} = 7.5 \cdot 10^{34}$ cm^{-2}s^{-1}. The goal of ATLAS Phase II Upgrade is to upgrade the detector to be able to take the full advantage of accelerator upgrade. The upcoming changes are firstly linked to the radiation damage, either the damage that the existing systems of detector have already suffered or from the fact that they will not be able to accept the fluences produced by HL-LHC. Secondly there are changes related to the increases in trigger rates and detector occupancy.

The bandwidth saturation of current ID occurs for $\langle\mu\rangle \cong 50$ hard proton-proton interactions per bunch crossing, corresponding to the peak luminosity of $\mathcal{L} = 2 \cdot 10^{34}$ cm^{-2}s^{-1}. The new tracking detector the ITk will be able to keep the same occupancy as ID with $\langle\mu\rangle \cong 200$ thanks to its increased granularity. The ITk will be newly also a part of the Track Trigger and the tracking information will be added to trigger objects provided by calorimeters and muon system. The trigger thresholds will be lowered which directly benefits the physics performance.

During the Long Shutdown 3, that is scheduled for the years 2024 - 2026, the whole Transition Radiation Tracker, Semiconductor Tracker and Pixel Detec-

tor will be removed and replaced with an all-silicon ITk. The ITk will consist of strip and pixel system. Both pixel and strip detectors will contain a barrel part and 2 end-cap parts placed on each side of the barrel, together covering $|\eta| = 4$. The schematic layout of the ITk is shown in Fig. 4.2. The new ATLAS Inner Tracker will show greater radiation hardness than the current ID. It should be able to withstand the radiation damage that is equivalent to integrated luminosity of 4000 fb^{-1}.

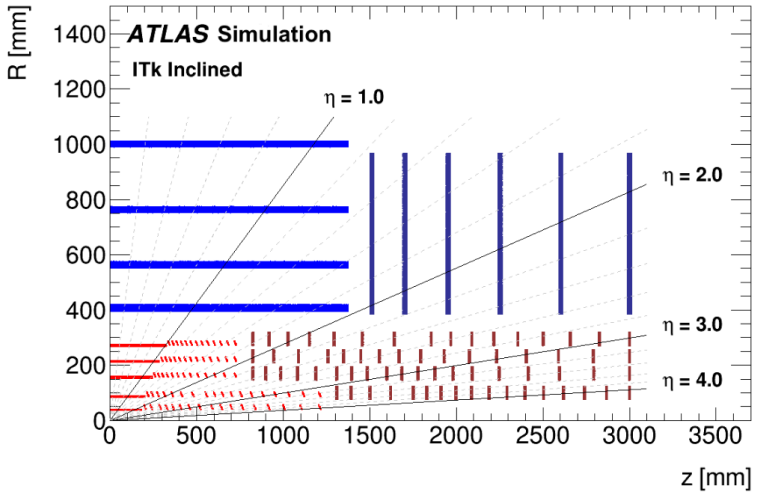

Figure 4.2: Schematic layout of the ITk for the HL-LHC phase of ATLAS [18].

4.4 Silicon Strip Detector

The silicon strip detector for the ITk is situated just outside the pixel detector with a silicon area ∼165 m^2. It consists of a central barrel region and two end-caps that extend the length of the ITk Strip Detector to $z = \pm$ 3 m. The strip barrel consists of four cylinders that surround the beam-line. The strip end-caps have six disks on each side to provide optimal coverage.

The four barrel layers consist of 392 staves with modules mounted on both sides. Each barrel stave is populated with 28 modules. In the end-caps each disk is populated with 32 identical petals. Each petal has nine modules on each side with six different sensor geometries to cover the wedge-shaped petal surface [10]. The end-cap petal and barrel stave is shown in Fig. 4.3.

The basic unit of the ITk Strip detector is the silicon strip module. A module consists of one sensor and one or two low-mass printed circuit boards (PCB), called hybrids, hosting the read-out ASICs. The modules are constructed by gluing hybrids to silicon sensors with electronic-grade epoxy. The short-strip barrel modules contain two hybrids, each with 10 ABCStar readout ASICs and 1 HCCStar control ASIC. The high voltage (HV) and low voltage (LV) is brought to the modules via the power board. Each power board includes HV Multiplexer, LV DC-DC convertor and Autonomous Monitoring and Control Chip (AMAC), which is monitoring the voltages, currents, temperatures and other characteristics of each module and is able to turn the module on and off.

Exploded view of a short-strip barrel module with all relevant components, long-strip barrel modules and end-cap modules feature the same component groups is shown in Fig. 4.4 [10].

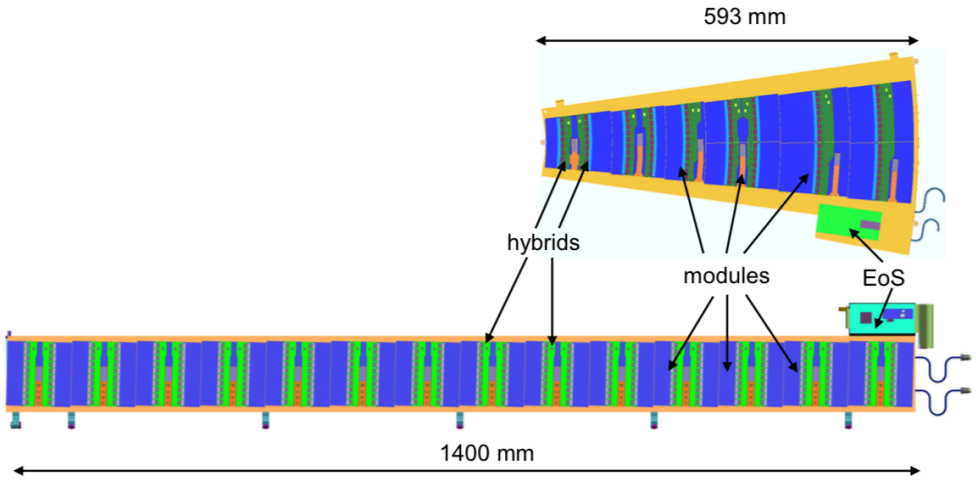

Figure 4.3: End-cap petal and barrel stave [10].

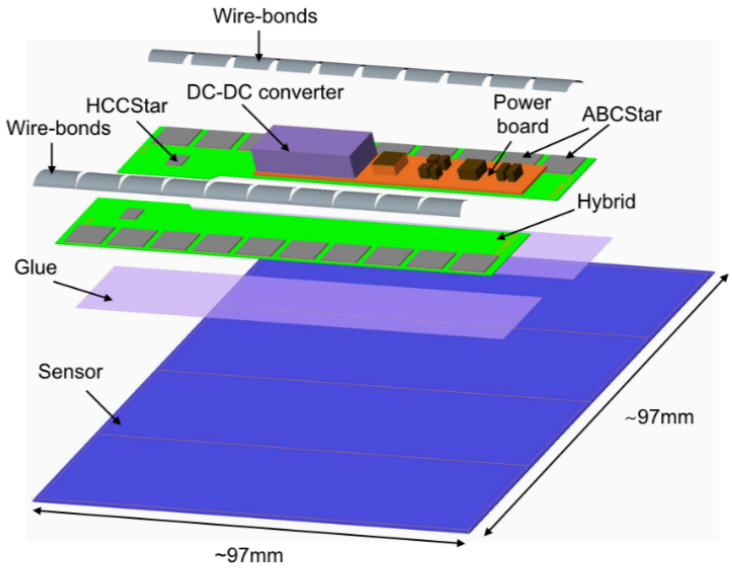

Figure 4.4: View of a short-strip barrel module [10].

4.5 Radiation Environment Expectations for the ITk

Due to the increased luminosity and the associated increase in the number of produced particles, the expected radiation levels in the ITk are significantly higher than for current ID. The simulation in Fig. 4.5 shows predicted total ionising doses (TID) in the ITk. The radiation background simulations were performed by using the FLUKA particle transport code [19] and the PYTHIA8 event generator [20]. The maximal TID absorbed in the strip part of the ITk detector is expected to be around 44 MRad (0.44 MGy), corresponding to the total fluence of 10.57 $\cdot 10^{14}$ MeV$\cdot n_{eq} \cdot cm^{-2}$ [21]. Using a standard safety factor 1.5 the maximum chosen gamma dose for the tested sensors was 70 MRad.

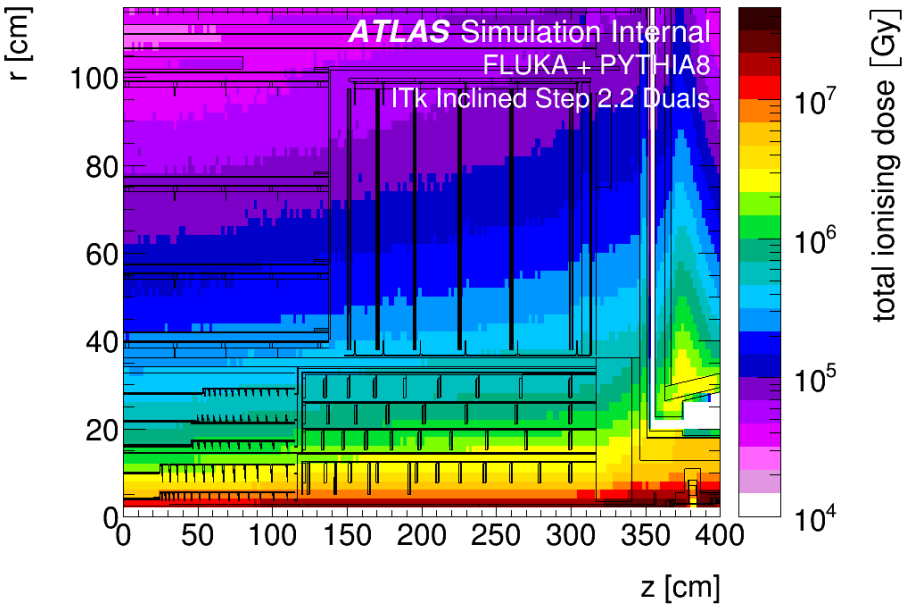

Figure 4.5: The total ionising dose for the ITk layout [21].

5. Sensor Characterization

Electrical tests were performed on the ATLAS17LS miniature (mini) sensors developed by the ATLAS ITk Strip Sensor Collaboration and produced by Hamamatsu Photonics. Sensors tested before and after irradiation provide a view on the impacts of gamma irradiation on their electrical parameters, while different received doses provide information on dependencies of electrical parameters on TIDs. The changes in leakage current and bulk capacitance are induced by bulk damage. The surface damage is visible in changes of interstrip resistance and capacitance, bias resistance and punch through protection efficiency.

The ATLAS17LS sensors are n^+-in-p type sensors that show better radiation hardness than p^+-in-n type sensors currently used in the ATLAS Inner Detector. The ATLAS17LS sensor specifications are listed in the table 5.1.

Table 5.1: Sensor specifications for the n^+-in-p type sensor [10].

Substrate material	
Type	p-type FZ
Thickness (physical)	300-320 μm
Thickness (active)	$\geq$ 90 % of physical thickness
Resistivity	$>$ 3 kΩcm
Sensor specifications before irradiation	
Full depletion voltage	$<$ 330 V
Maximum operating voltage	700 V
Poly-silicon bias resistors	1-2 MΩ
Inter-strip resistance	$> 10 \times R_{\text{bias}}$ at 300 V at 23 °C
Inter-strip capacitance	$<$ 1 pF/cm at 300 V, measured at 100 kHz
Coupling capacitance	$>$ 20 pF/cm at 1 kHz
Resistance of readout Al strips	$<$ 15 Ω/cm
Resistance of n-implant strip	$<$ 20 kΩ/cm
Total initial leakage current, including guard ring	$<$ 0.1 μA/cm^2 at 700 V at room temperature
Number of strips defects	$<$ 1 % per strip $<$ 1 % per sensor
After irradiation ($1.2 \cdot 10^{15}$ n_{eq}/cm^2 - 50 MRad)	
Onset of micro-discharge	$>$ 700 V or $V_{\text{fulldepletion}}$+ 50 V after irradiation (if lower)
Inter-strip resistance	$> 10 \times R_{\text{bias}}$ at 400 V and for T = -20 °C
Collected charge	$>$ 7500 electrons/MIP at 500 V

5.1 Sensor description

The tested sensors were ATLAS17LS mini 1×1 cm sensors and ATLAS17LS mini long strip (LS) 1×5 cm sensors. The sensors were part of the supply of ATLAS17LS strip sensors for the Step-3 of the Market Survey MS-4086/EP process of the ATLAS ITk Strip project.

Fig. 5.1 shows the wafer layout of ATLAS17LS sensors. All the sensors that were subject of our tests at IoP CAS are listed in the table 5.2.

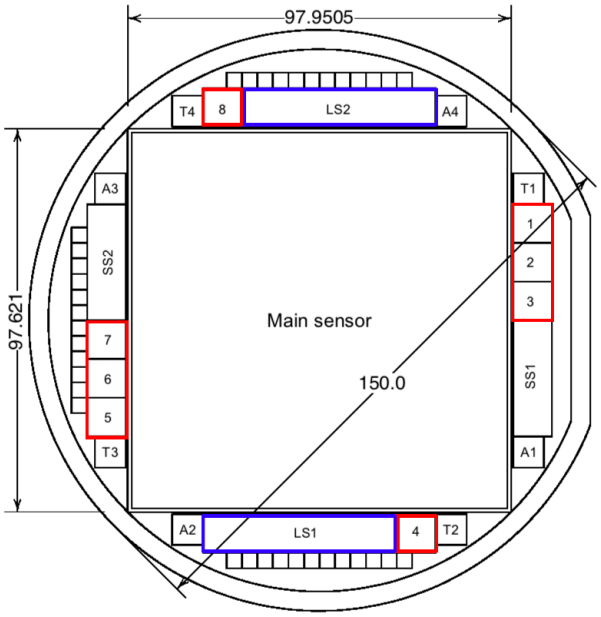

Figure 5.1: Wafer layout of ATLAS17LS main sensor and miniature sensors with marked mini 1×1 cm (red) and mini LS 1×5 cm (blue) sensors [22].

Table 5.2: List of tested sensors.

ATLAS17LS mini 1×1 cm	ATLAS17LS mini LS 1×5 cm
W0018 mini 2	W0018 slim dicing
W0018 mini 3	W0019
W0018 mini 4	W0020
W0018 mini 6	W0022 slim dicing
W0018 mini 7	W0025
W0022 mini 2 slim dicing	
W0022 mini 3 slim dicing	
W0022 mini 4 slim dicing	
W0022 mini 6 slim dicing	
W0022 mini 7 slim dicing	
W0004 mini 3	

5.2 Measurement setup

The electrical characteristics were measured on non-irradiated, irradiated and irradiated and annealed ATLAS17LS mini 1×1 cm sensors and non-irradiated, irradiated and irradiated and annealed ATLAS17LS mini LS 1×5 cm sensors.

The electrical characteristics of non-irradiated ATLAS17LS mini 1×1 cm and ATLAS17LS mini LS 1×5 cm, as well as of irradiated ATLAS17LS mini LS 1×5 cm and irradiated and annealed ATLAS17LS mini LS 1×5 cm sensors were measured at room temperature and normalized to 20 °C. The irradiated ATLAS17LS mini 1×1 cm and irradiated and annealed ATLAS17LS mini 1×1 cm sensors were tested in a freezer at ≈ -20 °C. The characteristics of each sensor were normalized to -20 °C.

When the characterization of the irradiated sensors was finished, the sensors were annealed and then tested once again. Annealing of all the sensors lasted for 80 minutes and the sensors were exposed to the temperature of 60 °C. Annealing heals the primary and secondary defects caused to the sensor by radiation, as by keeping the sensor at higher temperatures the radiation-generated damage may partially disappear, see Section 3.4.

The measurements at room temperature were performed at the semi automatic probestation Karl Suss PA 200, see Fig. 5.2. The probestation uses vacuum chuck with several openings that fix the sensor during contacting and the performed test. The chuck can be moved in three directions x, y and z by joystick. The precise focus for the operator while contacting the sensor is provided by Olympus microscope with the total magnification of 40× and an integrated CCD camera.

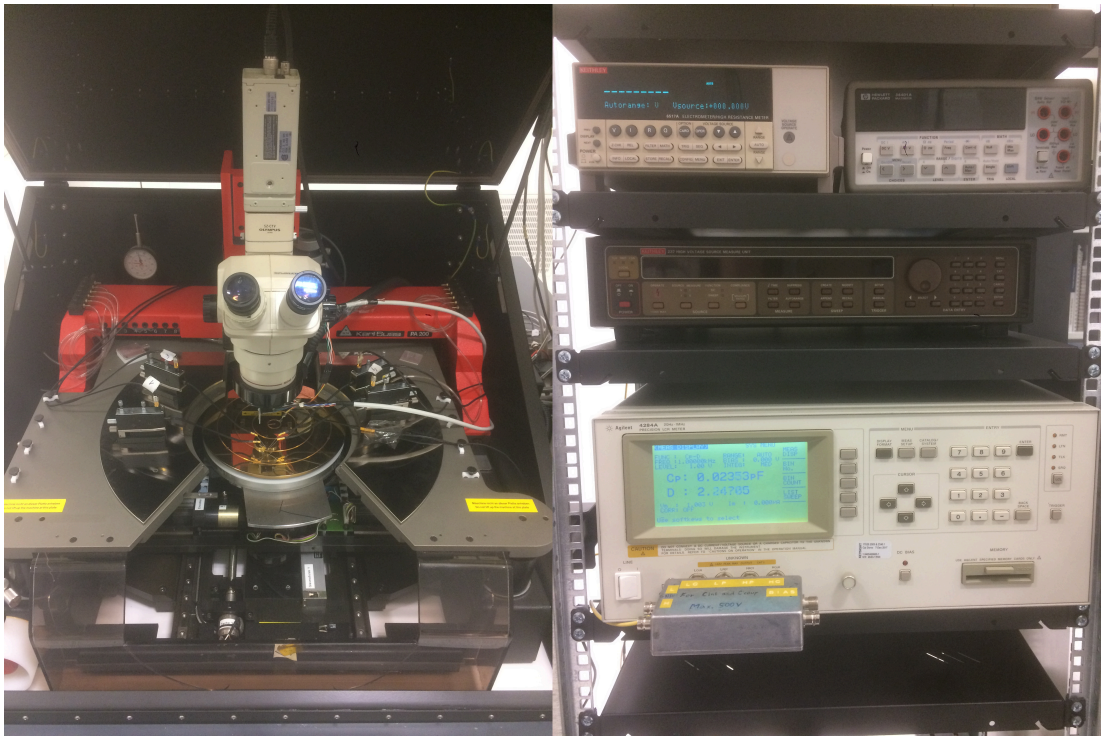

Figure 5.2: Semiautomatic probestation Karl Suss PA 200 (left) and the rack with electrical measurement devices (right).

The sensors pads are contacted by probes mounted on micro-manipulators, that are connected to the voltage source and measurement devices via coaxial cables with BNC connectors. The HV is applied on sensor via golden chuck of the probestation or a specially designed metal plate that is placed on the golden chuck. The whole probestation is placed in a dark metal box in order to protect the tested sensor from the electrical and optical noise from the surrounding environment.

The sensors tested in a freezer were wire bonded to the printed circuit boards (PCB's) that were especially designed for the tests by P. Mašek from the Institute of Experimental and Applied Physics of Czech Technical University in Prague. The AC and DC pads of three neighbouring strips, the bias ring pad and the high voltage pad were wire-bonded to the PCB. The contacts on the PCB were connected to the measurement devices by coaxial cables with LEMO connectors. Testing PCB with wire bonded sensor is shown in Fig. 5.3.

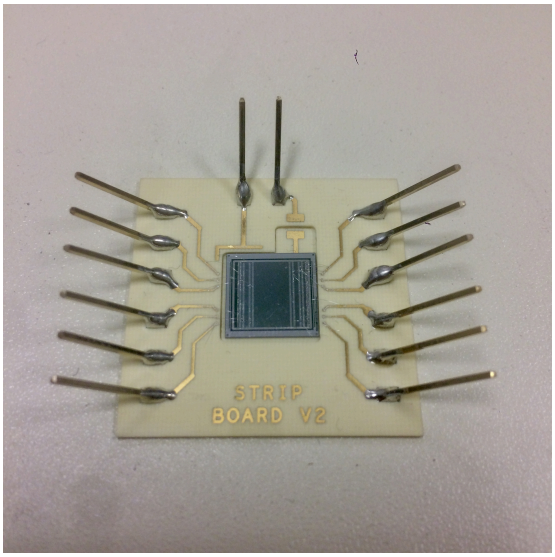

Figure 5.3: PCB with wire-bonded ATLAS17LS mini 1×1 cm.

The devices used for the tests are shown in Fig. 5.2. The high resistivity meter Keithley 6517A is in our studies used as HV source for biasing the tested sensor. Its range is from ± 5 mV to ± 1000 V [23]. The Source Measure Unit Keithley 237 provides voltage from ± 100 μV to ± 1000 V as a high-voltage source and simultaneously can be used for measurement of current or as a current source with the range from ± 100 fA to ± 100 mA [24]. We use it for current-voltage (IV) tests and for measurements of small interstrip currents. Keithley 487 picoammeter/voltage source is able to measure current between ± 10 fA and ± 2 mA and also can be used as a voltage source up to ± 500 V [25]. The LCR meter Hewlettt Packard (HP) 4284A provides testing frequencies from 20 Hz up to 1 MHz [26]. It was used for capacitance tests. Multimeter HP 34401A [27] was in our measurement setup used for measuring the resistance of the temperature sensor PT-100 [28].

All the devices listed above were connected to the computer and operated via General Purpose Information Bus (GPIB) by the LabView software developed by National Instruments Ltd [29].

5.3 Irradiation

The sensors were irradiated by gamma rays from Terabalt Cobalt-60 source at UJP Prague, see Fig. 5.4. During the irradiation, sensors were surrounded by 1.5 mm thick lead and 1.0 mm thick aluminium layers, which produced the charge particle minimizing the dose enhancement from low-energy scattered radiation [30]. The special holder with Pb and Al layers, that was designed and fabricated for the purpose of sensors irradiation at IoP CAS, ses Fig. 5.5. The dose profile of the Terabalt Cobalt-60 source is shown in Fig. 5.6. As we can see from the Fig. 5.6, the homogeneity in irradiation area of 6 cm is ±5%.

Figure 5.4: Terabalt Cobalt-60 source at UJP Prague [31].

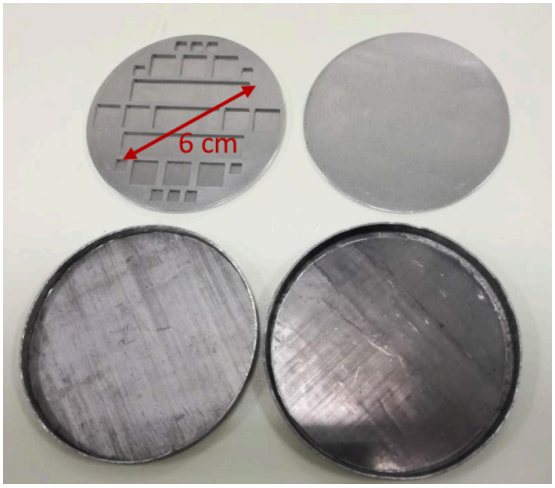

Figure 5.5: Holder for sensors irradiation.

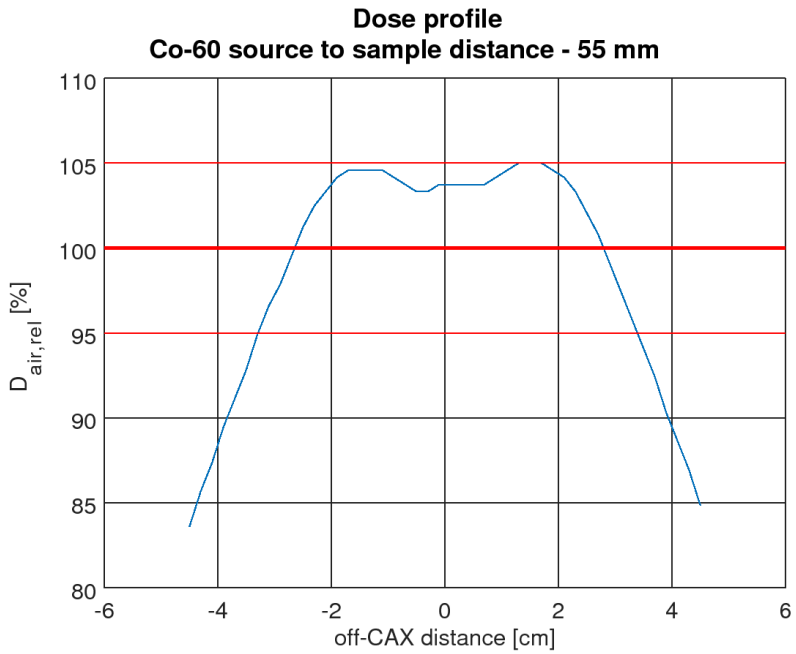

Figure 5.6: Dose profile of the Terabalt Cobalt-60 source installed at UJP Prague [31].

Table 5.3 contains dose rates and times of irradiation corresponding to each of TIDs. The temperature in the area of holder with the sensors was monitored during the irradiation and its dependence on time of irradiation is in Fig. 5.7. The radiation source was opened in the seventh minute and closed after 29 minutes of the temperature measurement. The temperature during the irradiation rises and stabilizes at ∼40 °C. The received total ionizing doses in tested silicon samples were 10 - 70 MRad as listed below in the table 5.4. The highest TID corresponds with the anticipated maximum TID received in strip area of the ITk multiplied by the safety factor of 1.5.

Table 5.3: Selected TID values with their corresponding rates and irradiation times.

TID [MRad]	Dose rate [kRad/min]	Time of irradiation [h]
10	24	7
17.5	24	12.2
35	24	24.3
52.5	24	36.5
70	22	53

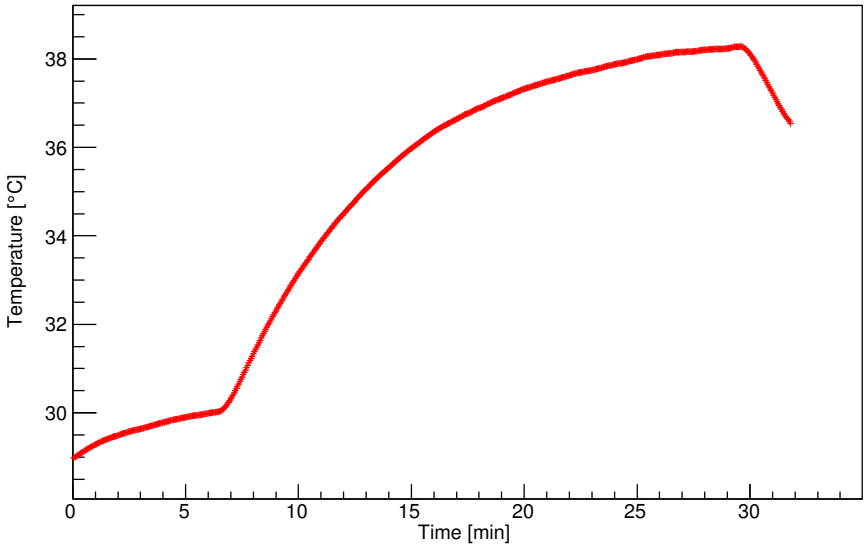

Figure 5.7: Dependence of temperature measured close to the sensor on the time during the irradiation of the sensors.

Table 5.4: Tested sensors and their received doses.

ATLAS17LS mini 1×1 cm	Dose [MRad]	ATLAS17LS mini LS 1×5 cm	Dose [MRad]
W0018 mini 2	70	W0018 slim dicing	70
W0018 mini 3	17.5	W0019	17.5
W0018 mini 4	52.5	W0020	35
W0018 mini 6	35	W0022 slim dicing	52.5
W0018 mini 7	10	W0025	10
W0022 mini 2 slim dicing	70		
W0022 mini 3 slim dicing	17.5		
W0022 mini 4 slim dicing	35		
W0022 mini 6 slim dicing	52.5		
W0022 mini 7 slim dicing	10		

5.4 Leakage current

The strips of the sensor behave like p-n diodes, that are reverse biased. The leakage current should show diode-like behavior and should become approximately constant after reaching the value of full depletion voltage.

The schematic of leakage current measurement setup is in Fig. 5.8. The high negative voltage is applied on the back-plane of the sensor and the leakage current is measured by contacting the bias pad. The measurement was performed using Keithley 237 High Voltage Source Measure Unit.

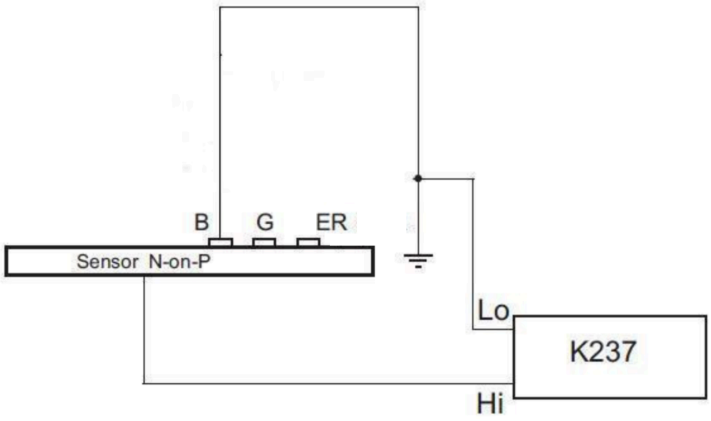

Figure 5.8: Schematic of leakage current measurement setup.

The obtained IV characteristics measured up to 700 V show constant value of leakage current well above the value of the full depletion voltage, see Figs. 5.9 and 5.10.

Fig. 5.9 shows that the value of measured current of ATLAS17LS mini LS 1×5 cm sensors is two orders of magnitude higher after irradiation. We can observe the dose dependence of leakage current, which increases with increasing received TID.

In Fig. 5.10, we can see that IV characteristics of ATLAS17LS mini 1×1 cm sensors don't show the dependence of the leakage current on received TID in contrast of IV characteristics of ATLAS17LS mini LS 1×5 cm sensors, where the dose dependence is clearly visible. Unobservable dose dependence for ATLAS17LS mini 1×1 cm sensors is caused by measurement inaccuracies, because we are not able to distinguish the changes in current that are under the resolution of measuring devices.

The value of measured current of irradiated ATLAS17LS mini LS 1×5 cm sensors is $10^3\times$ higher than the value of measured current of irradiated ATLAS17LS mini 1×1 cm due to different active volume of the sensors and the difference in the temperatures during the measurements.

Figs. 5.11 and 5.12 compare the IV characteristics of the sensors before and after annealing.

The leakage current of ATLAS17LS mini LS 1×5 cm sensors measured at 20 °C shows observable changes in its progress. Measured current decreases after annealing of the sensors for the lower voltages and then we can observe the increase of current for voltages higher than 400 V in comparison to the sensors

measured before annealing. The increase of current is probably created by surface current induced by annealing of the senors. Used measurement setup is not able to distinguish the surface and bulk current component.

The changes in leakage current of ATLAS17LS mini 1×1 cm sensors measured at -20 °C, shown in Fig. 5.12, are not observable due to the limited measurement resolution.

As mentioned in Section 3.1, gamma rays from Cobalt-60 source are absorbed in the sensor mainly through the Compton scattering and the recoil Compton electrons have high enough energy (hundreds of keV) to produce point defects in the Si bulk. Assuming that the observed increase of the leakage current with increasing TID is caused by the bulk damage, see Fig. 5.13, we can calculate for each TID value the equivalent fluence expressed in units of 1 MeV n_{eq}/cm^2 by using the equation 3.1. The obtained values are plotted in Fig. 5.14.

The equivalent fluence corresponding to the TID equal to 70 MRad has the value of $1.6 \cdot 10^{11}$ 1 MeV n_{eq}/cm^2, which is in good agreement with $1 \cdot 10^{12}$ 1 MeV n_{eq}/cm^2 estimated in [32].

The values of measured current in Fig. 5.13 are normalized to -20 °C using the equation 3.1. The inaccuracy in current measurement is mainly formed by the inaccuracy in temperature measurement that is ± 1 °C. Therefore, the resulting inaccuracy in current measurement is 11 %.

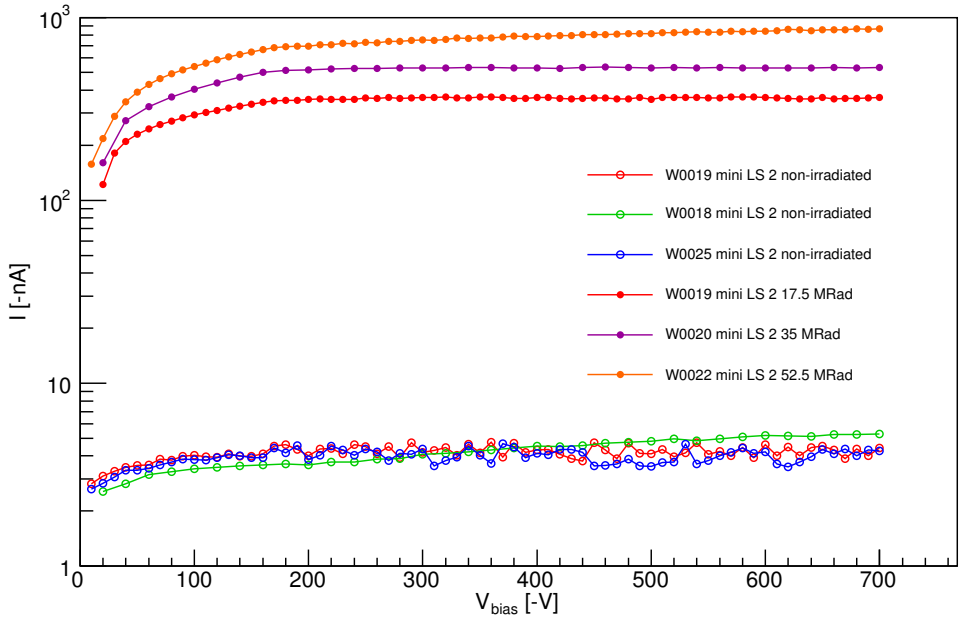

Figure 5.9: Comparison of IV characteristics for non-irradiated and irradiated ATLAS17LS mini LS 1×5 cm sensors measured at 20 °C.

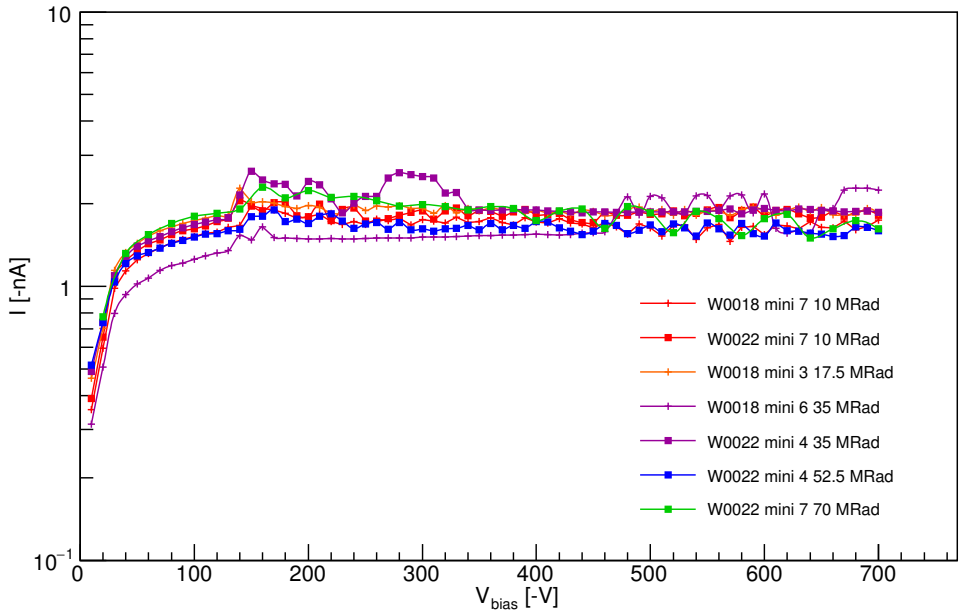

Figure 5.10: Leakage current as a function of V_{bias} of irradiated and annealed ATLAS17LS mini 1×1 cm sensors measured at -20 °C.

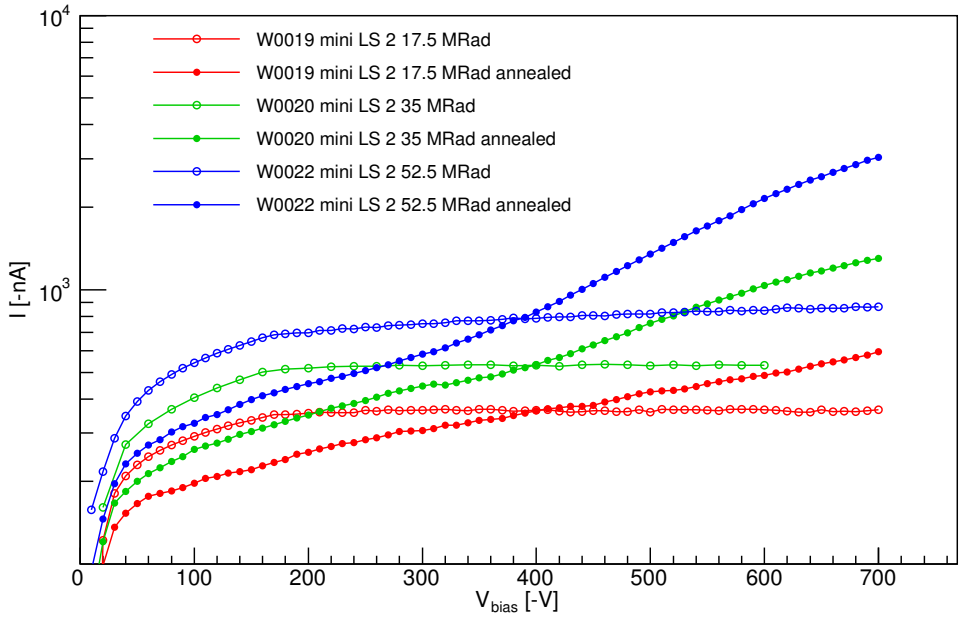

Figure 5.11: Comparison of IV characteristics for irradiated ATLAS17LS mini LS 1×5 cm sensors measured at 20 °C before and after annealing.

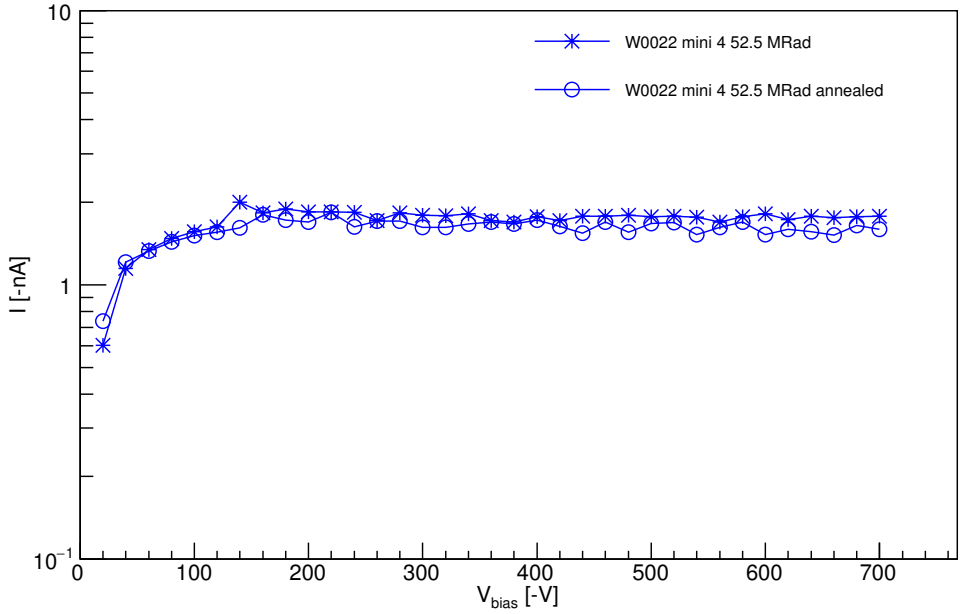

Figure 5.12: Comparison of IV characteristics for irradiated ATLAS17LS mini 1×1 cm sensors measured at -20 °C before and after annealing.

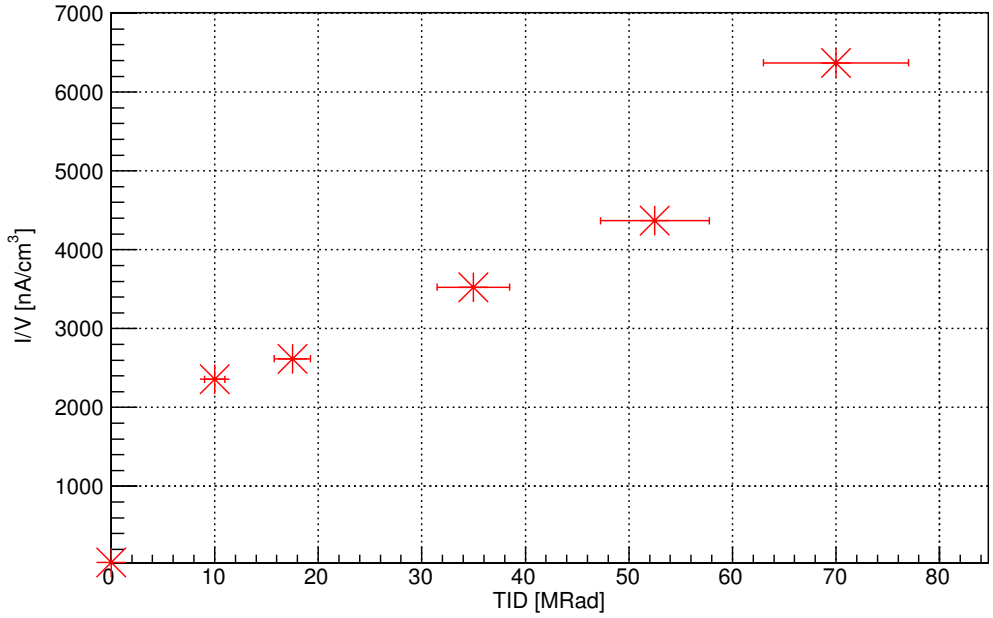

Figure 5.13: Dependence of the leakage current normalized to the unit sensor volume on the TID for irradiated and annealed ATLAS17LS mini LS 1×5 cm sensors measured at 20 °C.

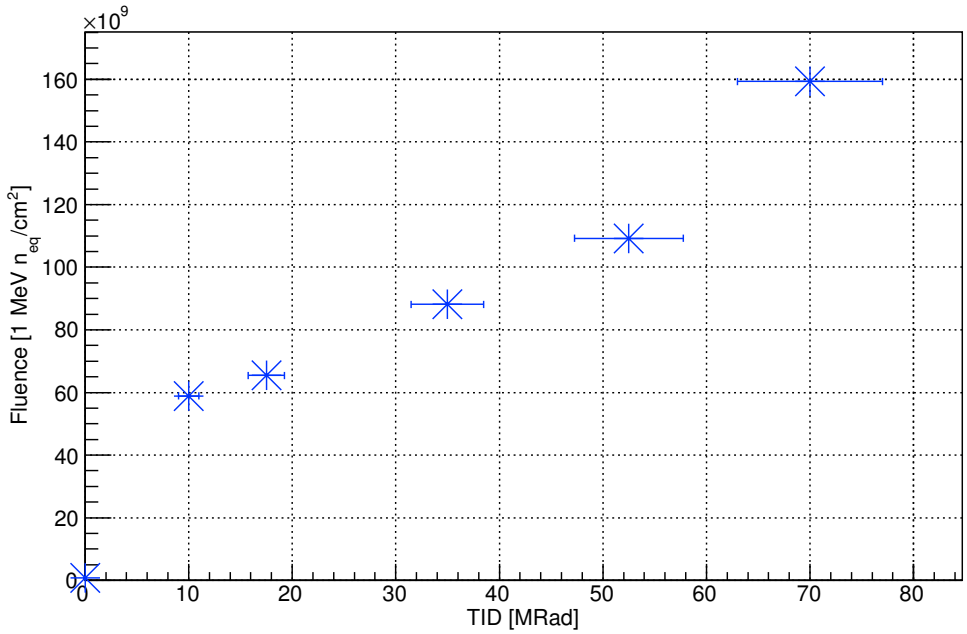

Figure 5.14: Equivalent fluence in units of 1 MeV n_{eq}/cm^2 calculated for individual TID values based on the Eq. 3.1.

5.5 Bulk Capacitance and Full Depletion Voltage

The bulk capacitance is the capacitance measured between the implant and the back-plane of the detector.

The bulk capacitance as a function of bias voltage was measured with a precision LCR meter HP 4284A at a frequency of 1 kHz to estimate the full depletion voltage of the detector. Fig. 5.15 shows the measurement setup that uses two protection boxes to protect the measurement electronics in case of sensors breakdown.

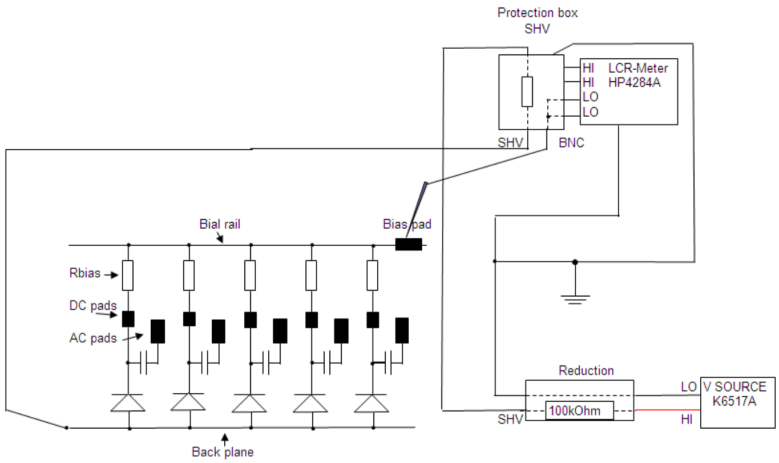

Figure 5.15: Schematic of bulk capacitance measurement setup.

Fig. 5.16 shows quantity $1/C^2$ as a function of bias voltage V_{bias} for non-irradiated ATLAS17LS mini LS 1×5 cm sensors. Bulk capacitance C_{bulk} decreases with the increasing bias voltage to the point when it reaches the value of full depletion voltage (FDV) and then remains constant value as the bias voltage continues to increase. ATLAS17LS mini LS 1×5 cm sensors have very uniform Capacitance-Voltage (CV) characteristics before irradiation. As follows from the formula 2.2, the linearity of $1/C^2$ below FDV indicates homogeneous effective doping concentration N_{eff} across the thickness of the sensor. N_{eff} is also uniform among all the tested sensors. The bulk capacitance C_{bulk} after depletion of the sensors before irradiation is (141.37 ± 0.54) pF and the FDV is (302 ± 4) V. The value of FDV was determined as the intersection of the fit of the linear dependence as the $1/C^2$ increases with increasing bias voltage and the fit of the constant $1/C^2$ graph area.

As seen from Fig. 5.17, after gamma irradiation C_{bulk} increases and depends on TID. The slope of $1/C^2$ changes too and indicates that irradiation changes effective doping concentration. Estimated values of FDV as a function of TID for ATLAS17LS mini LS 1×5 cm sensors and ATLAS17LS mini 1×1 cm sensors are plotted in Figs. 5.18 and 5.19, respectively. Measurements indicates that FDV of ATLAS17LS mini 1×1 cm sensors increases after irradiation and then decreases with increasing TID.

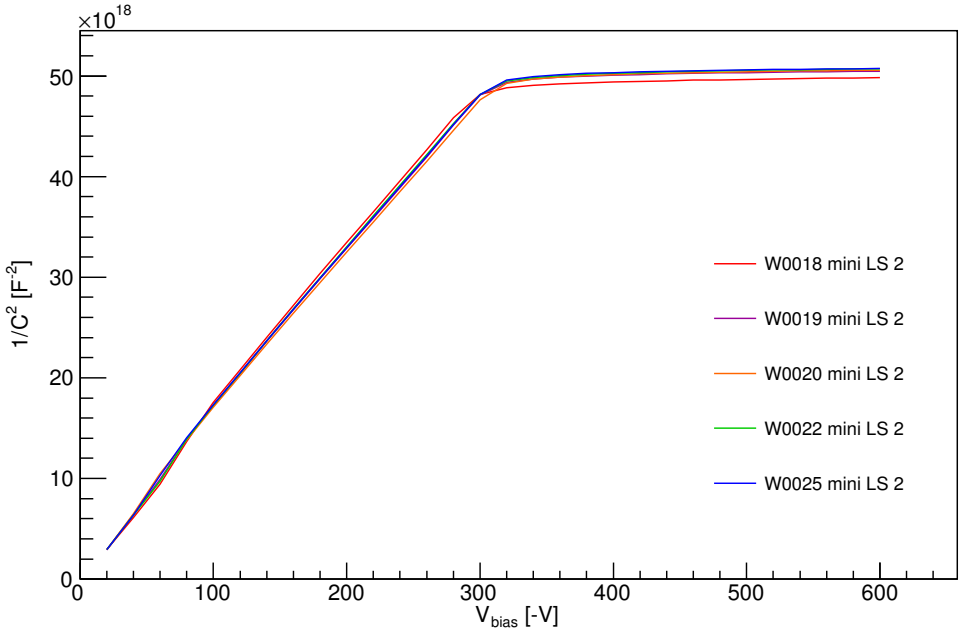

Figure 5.16: Quantity $1/C^2$ as a function of V_{bias} for non-irradiated ATLAS17LS mini LS 1×5 cm sensors measured at 20 °C.

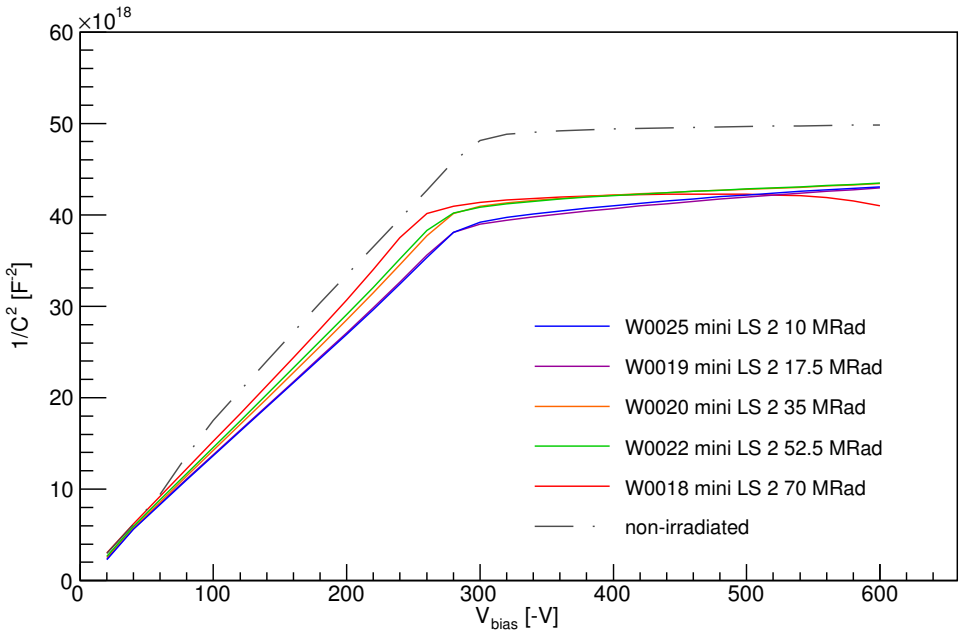

Figure 5.17: Quantity $1/C^2$ as a function of V_{bias} for irradiated ATLAS17LS mini LS 1×5 cm sensors and its comparison with $1/C^2$ for non-irradiated ATLAS17LS mini LS 1×5 cm sensors measured at 20 °C.

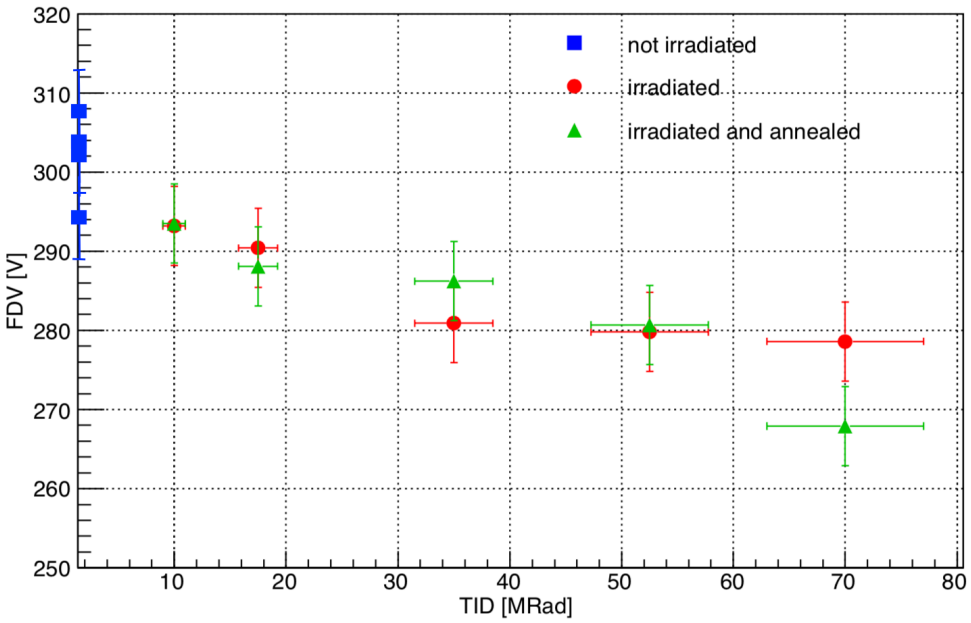

Figure 5.18: Dependence of FDV on TID for ATLAS17LS mini LS 1×5 cm sensors measured at 20 °C.

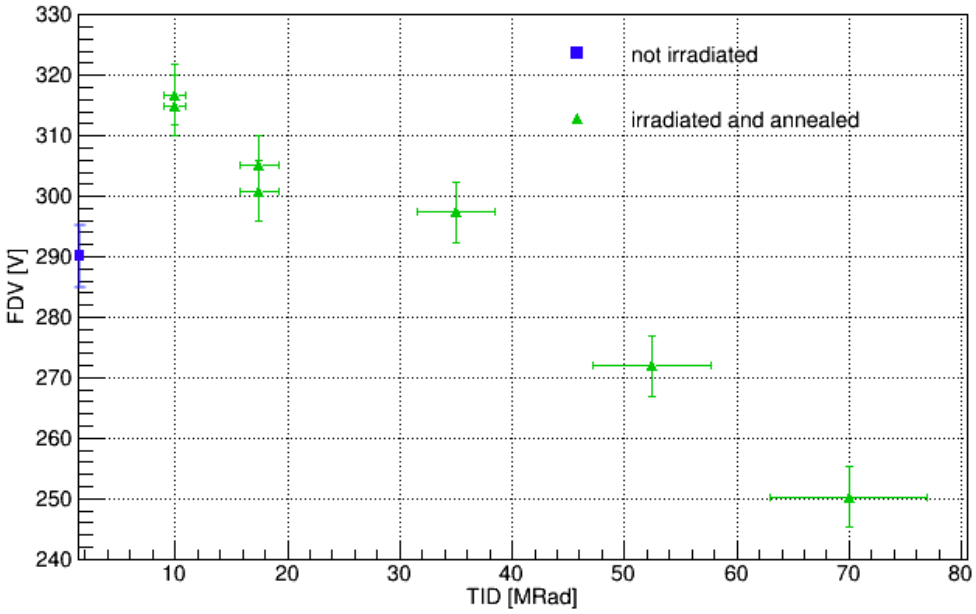

Figure 5.19: Dependence of FDV on TID for irradiated and annealed ATLAS17LS mini 1×1 cm sensors in comparison with non-irradiated one measured at -20 °C.

5.6 Interstrip Capacitance

The interstrip capacitance is the capacitance measured between a central strip and its nearest neighbours. The interstrip capacitance should be as low as possible, because it is the main part of the input capacitance of the front-end electronics and therefore of the detector noise.

The measurement of interstrip capacitance is performed by applying the high voltage on the back-plane of the sensor and then the interstrip capacitance is measured between AC strips, as shown in Fig. 5.20. The expected values of interstrip capacitance are in the order of several pF. That brings the need of precise corrections to the measurement to eliminate the parasitic capacitancies from the measuring electronics.

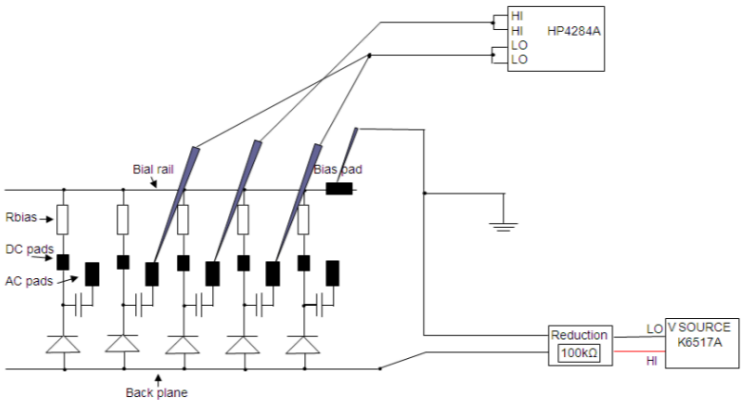

Figure 5.20: Schematic of interstrip capacitance measurement setup.

The interstrip capacitance is shown as a function of bias voltage in Fig. 5.21 for irradiated and annealed ATLAS17LS mini LS 1×5 cm sensors. It is obvious that interstrip capacitance decreases with increasing bias voltage. It is also dependent on TID for voltages under the full depletion voltage as it decreases with increasing TID.

The frequency dependence of interstrip capacitance at V_{bias}= -400 V is shown in Fig. 5.22. We can see that interstrip capacitance changes with test frequency and fixes constant for frequencies higher than 100 kHz. There is a resonance between 2 - 6 kHz that increases with increasing TID. The same effect was observed also in proton irradiated sensors [33].

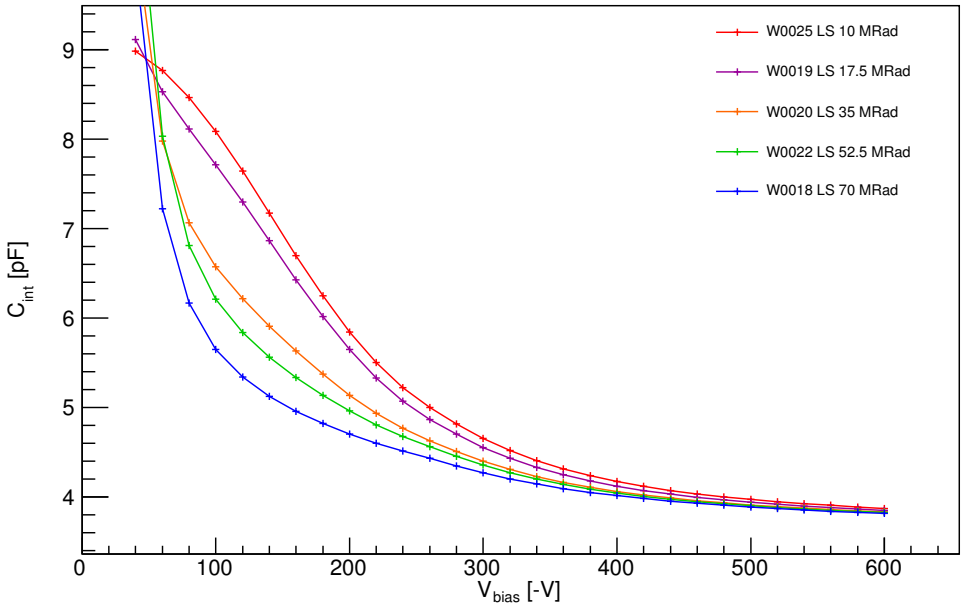

Figure 5.21: Interstrip capacitance as function of V_{bias} at $f = 1$ MHz for irradiated and annealed ATLAS17LS mini LS 1×5 cm sensors measured at 20 °C.

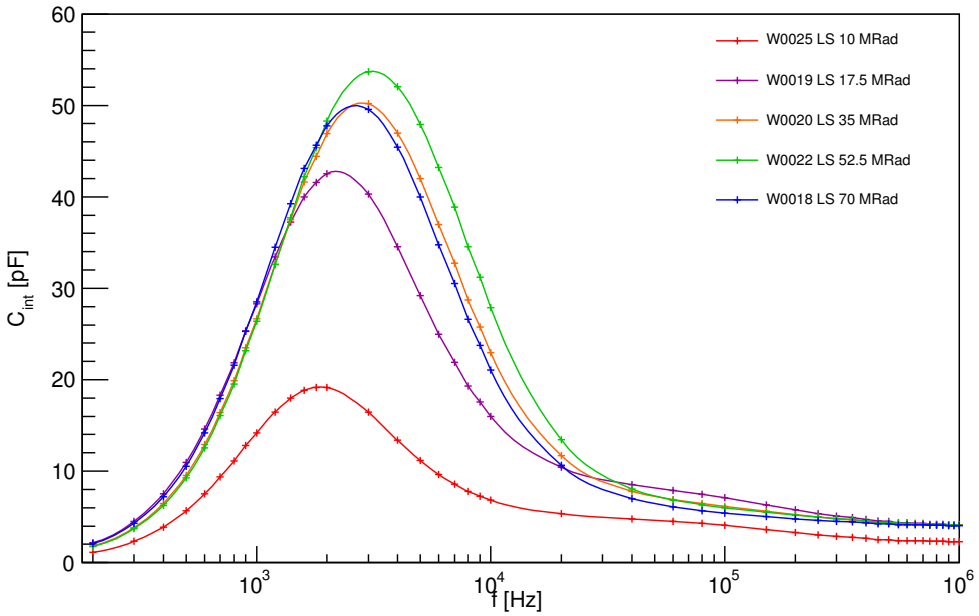

Figure 5.22: Frequency dependence of interstrip capacitance at V_{bias}= -400 V for irradiated and annealed ATLAS17LS mini LS 1×5 cm sensors measured at 20 °C.

5.7 Interstrip Resistance

The interstrip resistance is the resistance measured between neighbouring strips. Because of the low value of interstrip resistance, the signal from the two neighbouring strips can be shared between them and leads to the spatial resolution distortion of the detector.

According to the ATLAS specifications, listed in Tab. 5.1), the values of the interstrip resistance after irradiation should be $R_{\text{int}} > 10\times R_{\text{bias}}$ at 400 V for T= -20 °C.

The interstrip resistance was measured for bias voltage from -50 to -700 V in 50 V steps. As shown in Fig. 5.23, three neighbouring DC pads were contacted and the test voltage V_{applied} was applied on the two outer ones. The test voltage was chosen between -1 V and +1 V with the step of 0.4 V, when for each step the induced current I was measured on the middle pad. The interstrip resistance was determined by

$$R_{\text{int}} = 2\left(\frac{dI}{dV_{\text{applied}}}\right)^{-1}, \tag{5.1}$$

where dI/dV_{applied} is the slope of the line obtained by fitting the values of induced current I as a function of applied voltage V_{applied}.

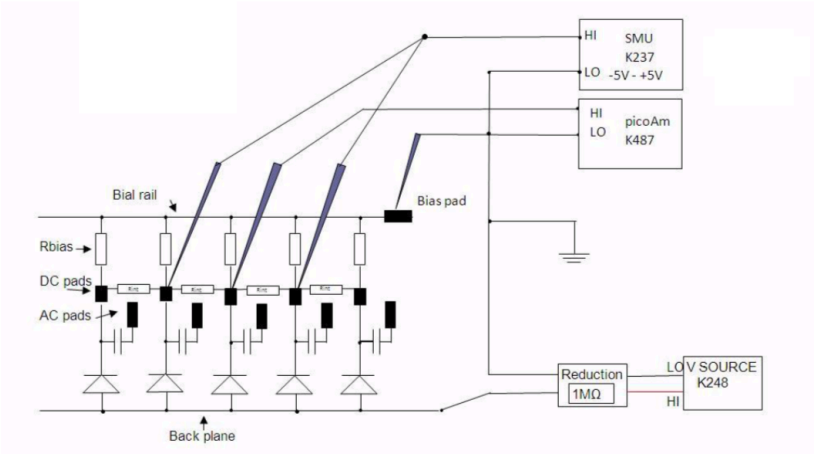

Figure 5.23: Schematic of interstrip resistance measurement setup.

The dependence of interstrip resistance R_{int} on bias voltage V_{bias} for ATLAS17LS mini 1×1 cm sensors irradiated by different TIDs is shown in Fig. 5.24. The interstrip resistance decreases with increasing TID.

The dependence of interstrip resistance on TID is shown in Fig. 5.25. The interstrip resistance strongly decreases with increasing TID. The values of interstrip resistance at V_{bias}= -400 V are decreasing from 2 GΩ for the dose of 10 MRad to 20 MΩ for 70 MRad.

Interstrip resistance of irradiated sensors is temperature dependent. The interstrip current has the same temperature dependence as bulk generation current [13]. Therefore, the measured values of interstrip resistance in Fig. 5.25 are normalized to -20 °C using the equation 3.1. The inaccuracy in values of interstrip

resistance is mainly formed by the inaccuracy in temperature measurement that is ± 1 °C. Thus, the resulting inaccuracy in interstrip resistance measurement is 11 %.

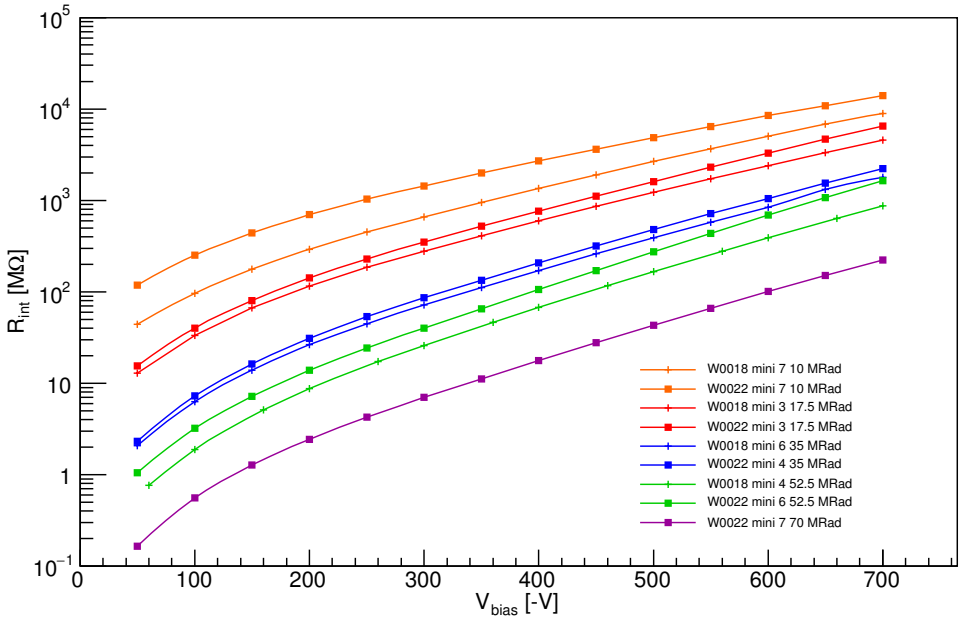

Figure 5.24: Interstrip resistance as a function of V_{bias} for irradiated and annealed ATLAS17LS mini 1×1 cm sensors measured at -20 °C.

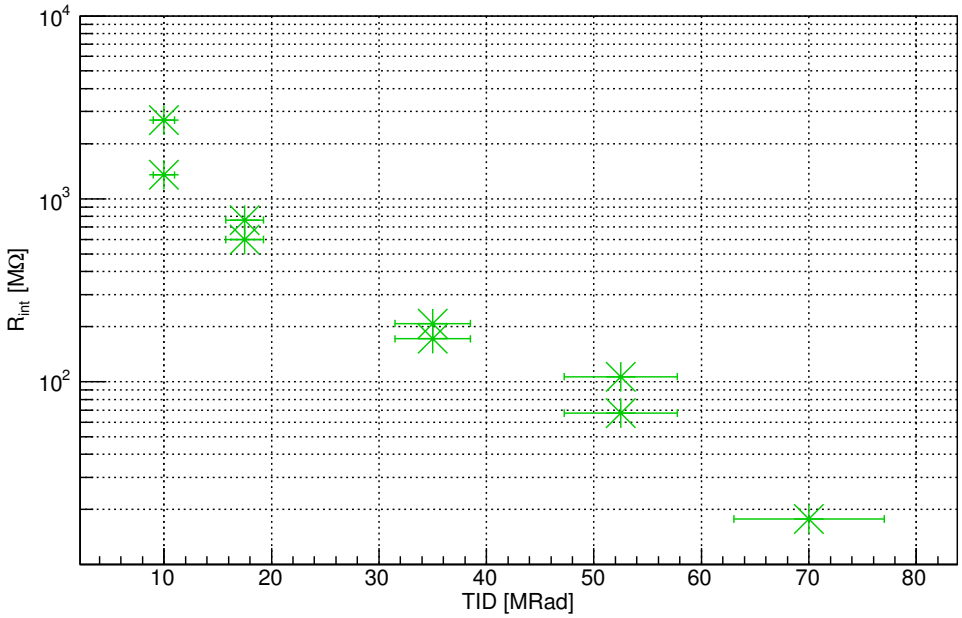

Figure 5.25: Dependence of interstrip resistance on TID at V_{bias}= -400 V for irradiated and annealed ATLAS17LS mini 1×1 cm sensors measured at -20 °C.

5.8 Coupling Capacitance

The coupling capacitance is the capacitance measured between the implant strip and metal readout strip which are separated from each other by SiO_2 layer.

Coupling capacitance can be determined using the equation for parallel plate capacitor

$$C = \epsilon_0 \epsilon_r \frac{A}{d}. \tag{5.2}$$

The value of coupling capacitance should be large, because the signal from the particle crossing the detector is proportional to the coupling capacitance. From equation 5.2 it results that the capacitance is higher when we have a thin dielectric layer d and a large strip width.

The coupling capacitance was measured while applying high voltage to the back-plane of the sensor by measuring the capacitance between DC and AC pads, see Fig. 5.26.

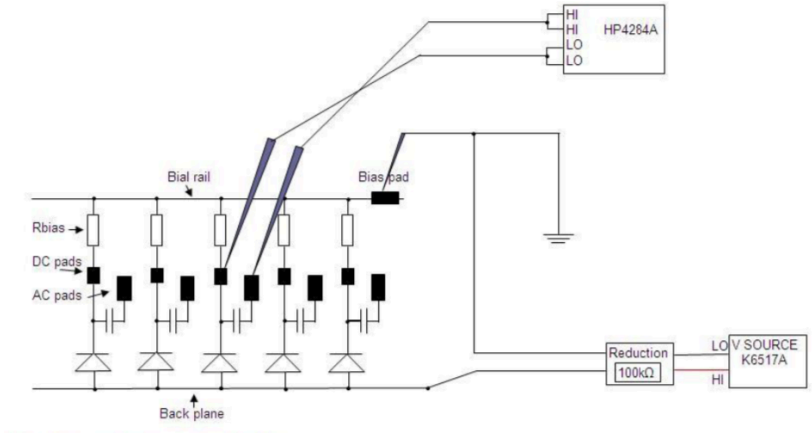

Figure 5.26: Schematic of coupling capacitance measurement setup.

Fig. 5.27 shows that coupling capacitance does not change after irradiation of the sensor. The values of coupling capacitance for ATLAS17LS mini 1×1 cm sensors are C_{coup} = (19.1 - 20.3) pF and the coupling capacitance per centimeter is then C_{coup}/cm = (23.9 - 25.4) pF/cm. As observable in Fig. 5.28, coupling capacitance C_{coup} does not depend on TID.

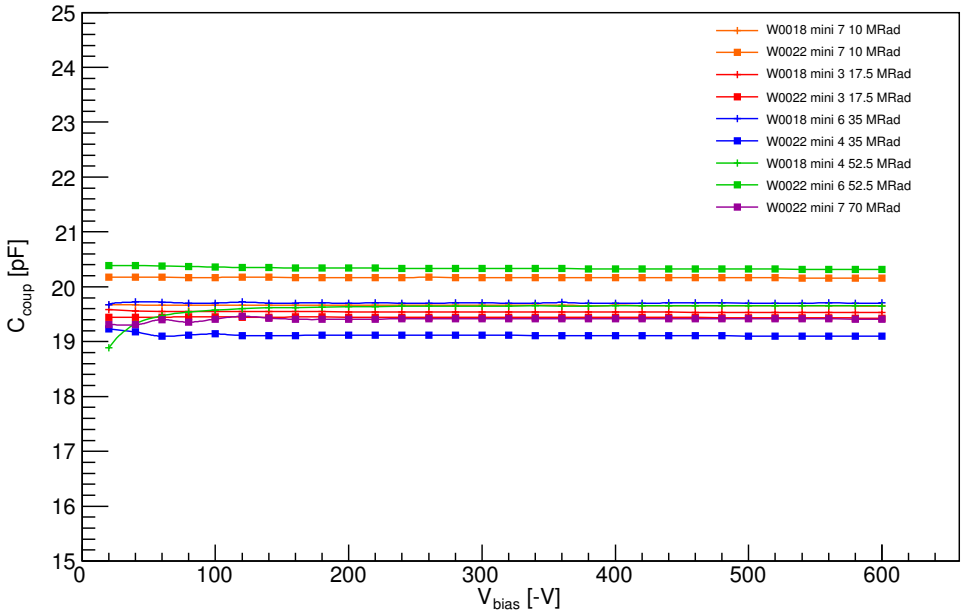

Figure 5.27: Coupling capacitance as a function of V_{bias} for irradiated and annealed ATLAS17LS mini 1×1 cm sensors measured at -20 °C.

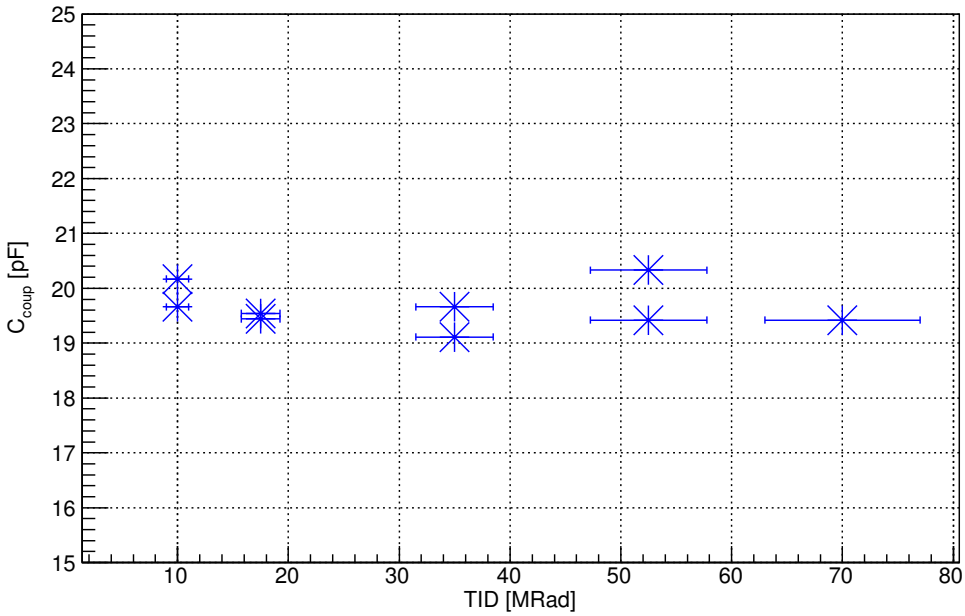

Figure 5.28: Dependence of coupling capacitance on TID at V_{bias}= -400 V for irradiated and annealed ATLAS17LS mini 1×1 cm sensors measured at -20 °C.

5.9 Punch Through Protection Effectiveness

Punch Through Protection (PTP) structure protects the implants and front-end electronics of modules against the enormous induced charge caused for example by accidental beam splash that would hit the tracker. PTP provides an alternative path to the unwanted charge to the ground. It is a low resistance path parallel to the bias resistor which is activated when the voltage across the layer of oxide exceeds a certain value.

PTP effectiveness was tested using the DC method [13] shown in the Fig. 5.29. The test voltage V_{test} is applied to the implant and increased in 1 V steps while measuring the current I_{test} through the bias resistor and PTP. The effective resistance R_{eff} is then determined as

$$R_{\text{eff}} = \frac{V_{\text{test}}}{I_{\text{test}}}. \tag{5.3}$$

The voltage at which the effective resistance decreases to one half of its original value is called punch through voltage (PTV).

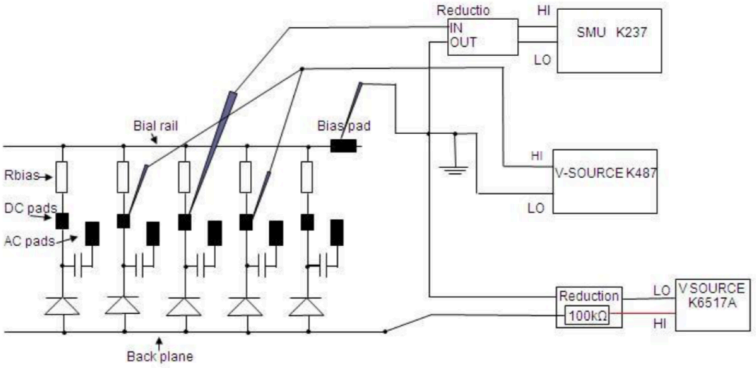

Figure 5.29: Schematic of PTP effectiveness setup.

Figs. 5.30 and 5.31 show the test current I_{test} and R_{eff} as a function of test voltage V_{test} for ATLAS17LS mini 1×1 cm sensors irradiated by different doses. The non-irradiated sensor is shown for comparison. We can observe that with increasing TID the PTP structure is more effective. Test current increases and the value of effective resistance decreases.

When we determine the PTV for the sensors, we can see that irradiation at first increases the value of PTV compared to the non-irradiated sensor. However, with the further increasing TID the value of PTV decreases and the PTP structure is more effective. Test current increases and the value of effective resistance decreases. Fig. 5.32 shows PTV as a function of TID. The initial increase of PTV is observed from 0 to 10 MRad, followed by a decrease with increasing TID.

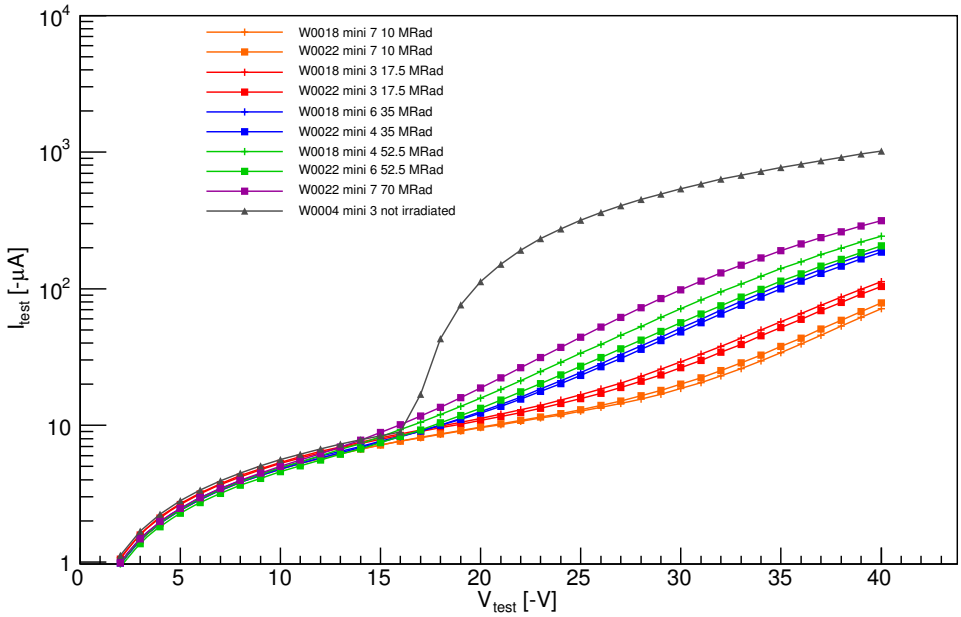

Figure 5.30: Test current I_{test} as a function of test voltage V_{test} for irradiated and annealed ATLAS17LS mini 1×1 cm sensors and its comparison with non-irradiated sensor measured at -20 °C.

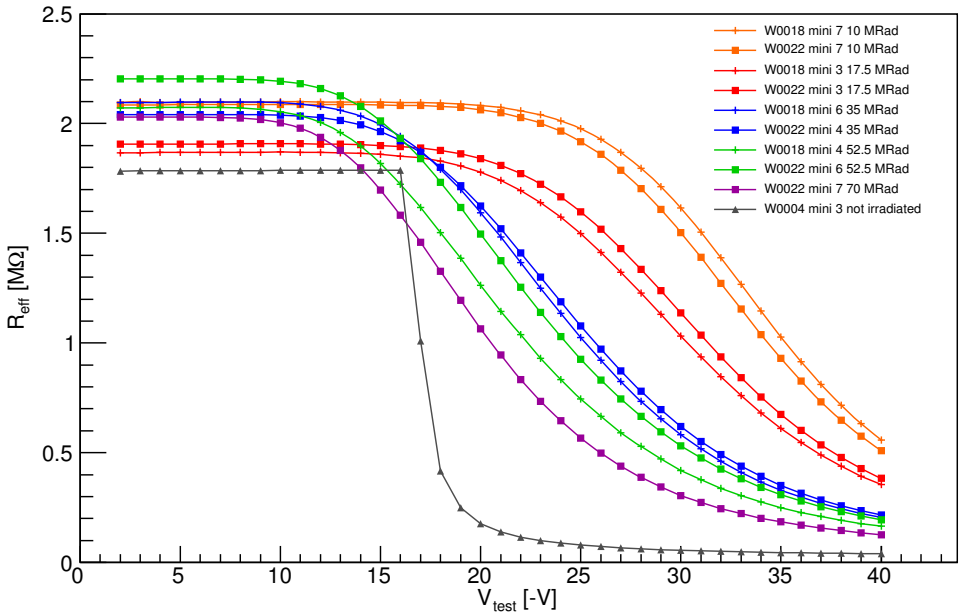

Figure 5.31: Effective resistance R_{eff} of the PTP structure as a function of test voltage V_{test} for irradiated and annealed ATLAS17LS mini 1×1 cm sensors and its comparison with non-irradiated sensor measured at -20 °C.

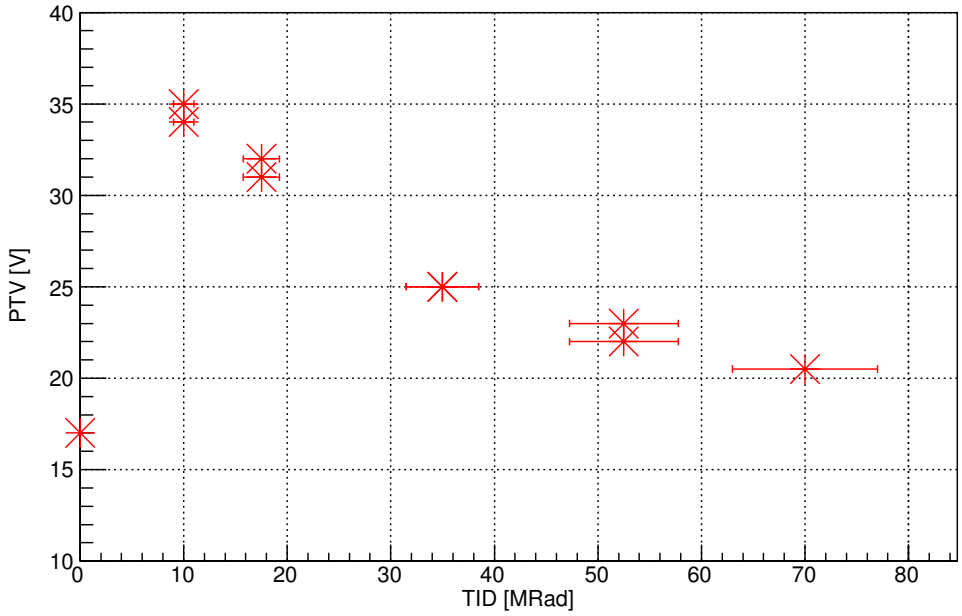

Figure 5.32: Dependence of PTV on TID at V_{bias}= -600 V for irradiated and annealed ATLAS17LS mini 1×1 cm sensors and its comparison with non-irradiated sensor measured at -20 °C.

5.10 Polysilicon Bias Resistance

The implant strips are connected to the bias ring by the polysilicon bias resistors.

The bias resistance is usually measured as a function of bias voltage by 1-probe method. The test voltage V_{applied} is applied between the implant strip and the grounded bias rail. The IV measurement is performed in range (-1,1) V to determine bias resistance R_{bias}.

As previously shown in 5.7 gamma irradiated sensors have much lower interstrip resistance. Therefore, interstrip currents and some extra current from the bulk influence the bias resistance measurements. To eliminate interstrip effects in gamma irradiated sensors the test voltage was applied also on two neighbours (3-probes method) at the same time, see Fig. 5.33. The measurement of current I was performed only on the central strip [13]. The main advantage of the 3-probes method is that, when were are applying the voltage on the neighbouring strips, there is no leakage of measured current on them. The polysilicon bias resistance is then determined using

$$R_{\text{bias}} = \left(\frac{dI}{dV_{\text{applied}}} \right)^{-1}, \tag{5.4}$$

where dI/dV_{applied} is the slope of the line obtained by fitting the values of induced current I as a function of applied voltage.

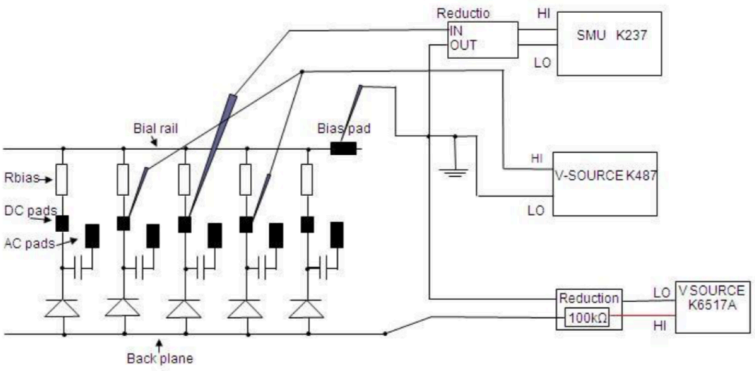

Figure 5.33: Schematic of polysilicon bias resistance setup.

Fig. 5.34 shows polysilicon bias resistance R_{bias} as a function of bias voltage V_{bias} in range (-100, -700) V for ATLAS17LS mini 1×1 sensors irradiated by different doses. No bias voltage dependence was observed. Differences of R_{bias} are probably caused by slightly different measurement temperatures.

Fig. 5.35 shows polysilicon bias resistance as a function of TID for ATLAS17LS sensors 1x1 cm at bias voltage V_{bias}= -400 V. The values of polysilicon bias resistance of irradiated sensors are in range (1.8 - 2.02) MΩ and do not change with TID.

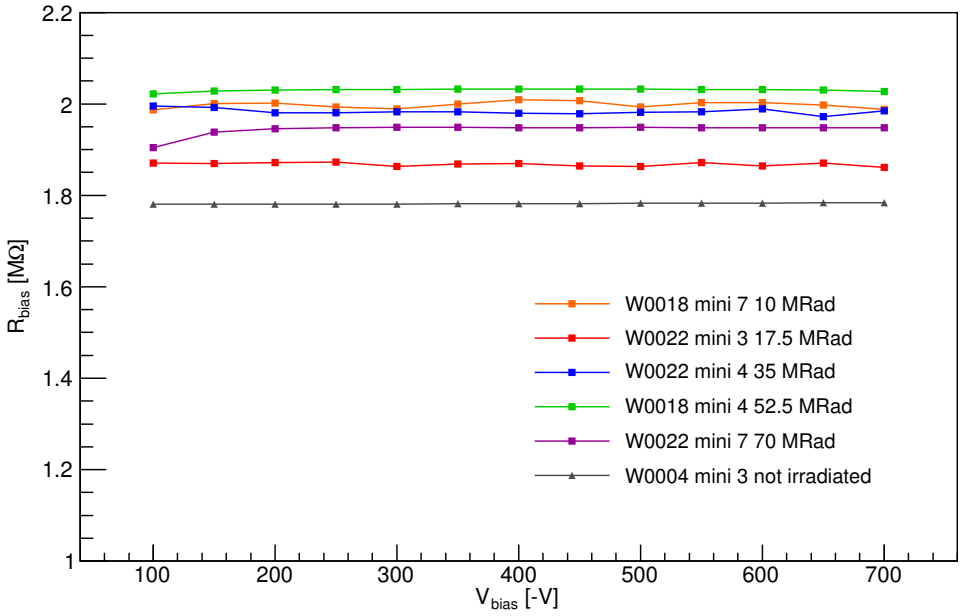

Figure 5.34: Polysilicon bias resistance as a function of V_{bias} for irradiated and annealed ATLAS17LS mini 1×1 cm sensors measured at -20 °C.

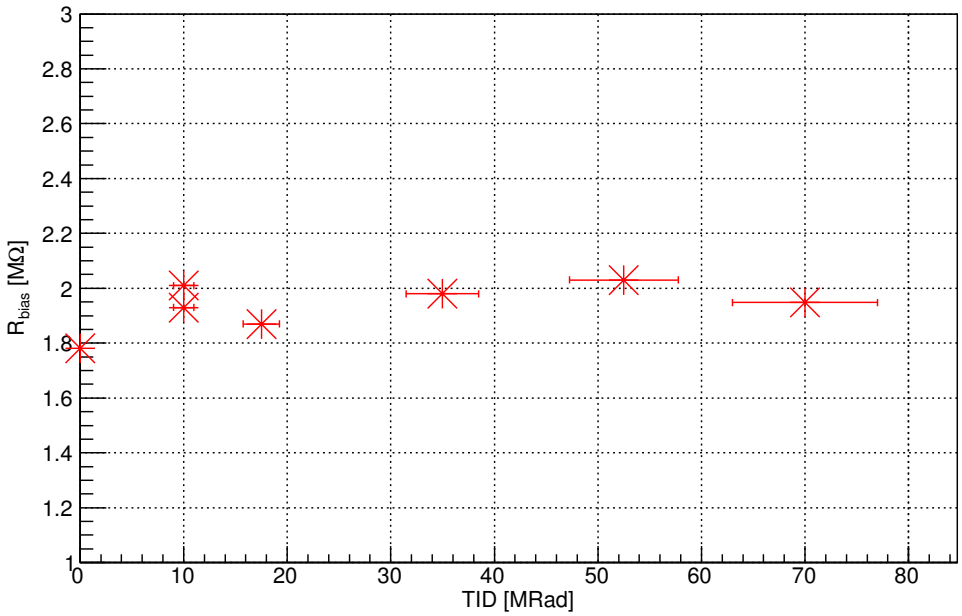

Figure 5.35: Dependence of polysilicon bias resistance on TID at V_{bias}= -400 V for irradiated and annealed ATLAS17LS mini 1×1 cm sensors measured at -20 °C.

Conclusion

The effects of radiation damage on detection performance of silicon strip sensor were studied. The tested sensors were n^+-in-p type sensors ATLAS17LS, the newest prototypes of strip sensors developed by ATLAS ITk Strip collaboration for use in new ATLAS Inner Tracker. The sensors will replace micro-strip sensors made with p-strips implanted on n-type silicon bulk (p^+-in-n) currently used in ATLAS Inner Detector. The replacement will be realized during the ATLAS Phase II Upgrade, that results from the upgrade of LHC into HL-LHC and its increased luminosity that gives greater demands on radiation hardness of detection systems. The current ID will not be able to withstand newly created radiation environment while maintaining its required detection performance. The n^+-in-p type sensors developed for the strip detector of new all-silicon ITk, are more radiation hard. Sensors are single-sided with AC-coupled readout and n-strips are biased through polysilicon resistors. The substrate is high resistivity p-type silicon. Sensors were produced by Hamamatsu Photonics in a 6-inch (150 mm) wafer. Besides the real sized large sensor with the area of $\sim$10×10 cm^2, the wafer also includes sets of miniature sensors, which have a design similar to the real sized sensor apart from the differences consequential on a reduced sensitive area (number of strips or strip length). The tested miniature sensors had 128 strips of length 1 cm (ATLAS17LS mini 1×1 cm) and 5 cm (ATLAS17LS mini LS 1×5 cm) and were fully diced from the wafer.

The study of effects of the radiation damage on the detection performance of ATLAS17LS sensors took place in the clean laboratory of IoP CAS. The electrical properties of non-irradiated ATLAS17LS mini sensors were compared with gamma irradiated ones. The irradiation of the sensors was accomplished by the Terabalt Cobalt-60 source at UJP Praha. The received doses were 10, 17.5, 35, 52.5 and 70 MRad, where 70 MRad corresponds to the highest value of TID to be delivered to the ATLAS ITk strip detector during the HL-LHC operation, including the safety factor 1.5.

Non-irradiated, irradiated and irradiated and annealed ATLAS17LS mini LS 1×5 cm sensors and non-irradiated ATLAS17LS mini 1×1 cm sensors were tested in semi automatic probestation Karl Suss PA 200 at room temperature, while the irradiated and irradiated and annealed ATLAS17LS mini 1×1 cm sensors were tested in a freezer at $\approx$ -20 °C. Testing pads of sensors measured in probestation were contacted by probes electrically connected to measuring devices. The sensors tested in a freezer were wire-bonded to the PCBs that were especially designed for the tests. Measurements of irradiated sensors were performed before and after the controlled annealing at 60 °C for 80 minutes.

The obtained IV characteristics before and after gamma irradiation show smooth behaviour well above the value of the full depletion voltage. No breakdown voltage was observed up to the maximum tested bias voltage 700 V. The total leakage current increases $\sim$100× after gamma irradiation. The values of leakage current of ATLAS17LS mini LS 1×5 cm sensors measured at room temperature increases with increasing TID. Unfortunately, this dependence was not observable for ATLAS17LS mini 1×1 cm sensors measured at -20 °C mainly because the changes of leakage current were under the resolution of measurement

setup. The bulk capacitance and the full depletion voltage of all the sensors before irradiation can be considered as the same. It indicates the homogeneous effective doping concentration and the similar active thickness among all the tested sensors. After irradiation the values of FDV decrease with increasing TID for both the ATLAS17LS mini LS 1×5 cm and ATLAS17LS mini 1×1 cm sensors. The changes in the leakage current and bulk capacitance after gamma irradiation indicate radiation induced bulk damage. Gamma rays from Co-60 source are absorbed in the sensor mainly through the Compton scattering and the recoil Compton electrons have high enough energy to produce point defects in the silicon bulk.

The surface damage caused to the sensors is observable in changes of interstrip resistance and capacitance, polysilicon bias resistance and punch through protection efficiency. The interstrip capacitance of ATLAS17LS mini LS 1×5 cm sensors decreases with increasing bias voltage and depends on TID for voltages under the full depletion voltage as it decreases with increasing TID. The interstrip resistance of ATLAS17LS mini 1×1 cm sensors strongly decreases with increasing TID. The coupling capacitance does not depend on the TID. The value of PTV decreases with the increase of TID and PTP structure is more effective with increasing ionizing dose. The resistance of polysilicon bias resistors does not change with irradiation. The values of polysilicon bias resistance were approximately 2 MΩ for all the ATLAS17LS mini 1×1 sensors measured at -20 °C and meet the ATLAS specifications.

Measured characteristics provide a view on impacts of gamma irradiation on detection performance of ATLAS17LS silicon strip sensors. The results were presented on Strip Sensor Meeting at CERN by the author.

All the measured characteristics of ATLAS17LS sensors are in agreement with technical requirements of ATLAS ITk project. ATLAS17LS sensors satisfy the ATLAS ITk Strip collaboration detection performance requirements and they can be used in ATLAS ITk strip detector.

Bibliography

[1] The Higgs boson. https://atlas.cern/discover/detector. [Accessed: 2019-04-17].

[2] Z. Doležal. Experimental Methods of Nuclear and Subnuclear Physics. http://ipnp.cz/dolezal/teach/expmet/expmet.pdf, Feb 2019. [Accessed: 2019-04-19].

[3] S. Tavernier. *Experimental Techniques in Nuclear and Particle*. Springer-Verlag, Berlin Heidelberg New York, 2010.

[4] Cobalt-60 decay scheme. https://upload.wikimedia.org/wikipedia/commons/thumb/e/e0/Cobalt-60_Decay_Scheme.svg/1152px-Cobalt-60_Decay_Scheme.svg.png. [Accessed: 2019-04-17].

[5] G. Lutz. *Semiconductor Radiation Detectors*. Second printing. Springer-Verlag, Berlin Heidelberg New York, 2001.

[6] M. Mikeštíková. Vývoj přesných souřadnicových detektorů pro Vnitřní detektor experimentu ATLAS. *Dissertation, Faculty of Nuclear Sciences and Physical Engineering, Czech Technical University in Prague*, 2000.

[7] M. Moll. Radiation damage in silicon particle detectors - microscopic defects and macroscopic properties. *Dissertation, University Hamburg*, 1999.

[8] A. Koutoulaki. The ITk strips tracker for the phase-II upgrade of the ATLAS detector of the HL-LHC. http://www.bo.infn.it/sminiato/sm16/04_Giovedi/Mattina/08_Koutoulaki.pdf, Oct 2016. [Accessed: 2019-02-17].

[9] Market survey technical description planar silicon sensors for the ATLAS and CMS outer tracker upgrades. https://cds.cern.ch/record/2145271/files/MS-4086_Technical_Description.pdf. [Accessed: 2019-02-27].

[10] ATLAS Collaboration. *Technical design report for the ATLAS Inner Tracker strip detector*. tech. rep. CERN-LHCC-2017-005. ATLAS-TDR-025. CERN, Geneva, Apr. 2017.

[11] H. Spieler. *Semiconductor detector systems*. OUP Oxford, Series on Semiconductor Science and Technology, 2005.

[12] G. Lindström. Radiation Damage in Silicon Detectors. *Nucl. Instr. and Meth.*, A 512, 30, 2003.

[13] M. Mikeštíková et al. Study of surface properties of ATLAS12 strip sensors and their radiation resistance. *Nuclear Instruments and Methods in Physics Research Section A: Accelerators, Spectrometers, Detectors and Associated Equipment*, 831, 197–206, 2016.

[14] M. Moll. Displacement damage in silicon detectors for high energy physics. *IEEE Transactions on Nuclear Science*, 1-1, 2018.

[15] G. Lindström M. Moll E. Fretwurst, G. Kuhnke. Radiation hardness of silicon detectors for applications in high-energy physics experiments. *Journal of Optoelectronics and Advanced Materials*, 2000.

[16] Detector and Technology. `https://atlas.cern/discover/detector`. [Accessed: 2019-03-13].

[17] J. Pequenao. Computer generated image of the whole ATLAS detector. `https://cds.cern.ch/images/CERN-GE-0803012-01`, Mar 2008. [Accessed: 2019-02-19].

[18] ATLAS Collaboration. *Technical Design Report for the ATLAS Inner Tracker Pixel Detector*. tech. rep. CERN-LHCC-2017-021. ATLAS-TDR-030. CERN, Geneva, Jun. 2018.

[19] Fluka. `http://www.fluka.org/fluka.php?id=man_onl&sub=7`. [Accessed: 2019-05-06].

[20] Pythia8. `http://home.thep.lu.se/~torbjorn/Pythia.html`. [Accessed: 2019-05-06].

[21] Radiation Background Simulations Step 2X. `https://twiki.cern.ch/twiki/bin/viewauth/Atlas/RadiationBackgroundSimulationsStep2X`, Jan 2019. [Accessed: 2019-02-26].

[22] The ATLAS ITk Strip Sensor Collaboration. Technical Specification for the Supply of ATLAS17LS Strip Sensors. `https://indico.cern.ch/event/592256/contributions/2390452/attachments/1388483/2121025/ATLAS17LSTechnicalSpecsR1.3.pdf`, Jun 2017. [Accessed: 2019-03-16].

[23] Model 6517A Electrometer User's Manual. `http://download.tek.com/manual/6517A_900_01C.pdf`. [Accessed: 2019-03-16].

[24] 237 High Voltage Source-measure Unit. `https://www.tek.com/datasheet/model-237-high-voltage-source-measure-unit`. [Accessed: 2019-03-16].

[25] Keithley 487 Datasheet. `http://www.testequipmenthq.com/datasheets/KEITHLEY-487-Datasheet.pdf`. [Accessed: 2019-03-16].

[26] HP 4284A precision LCR Meter Operation Manual. `https://wiki.epfl.ch/carplat/documents/hp4284a_lcr_manual.pdf`. [Accessed: 2019-03-16].

[27] HP34401A Multimeter. `http://ecee.colorado.edu/~mathys/ecen1400/pdf/references/HP34401A_BenchtopMultimeter.pdf`. [Accessed: 2019-05-06].

[28] PT-100 Sensors. `https://www.ojelectronics.com/business-areas/hvac-controls-power/products/pt-100-sensors-prod90`. [Accessed: 2019-05-06].

[29] Labview. `http://czech.ni.com/labview`. [Accessed: 2019-04-19].

[30] Subcommittee E10.07 on Radiation Dosimetry for Radiation Effects on Materials and Devices. Standard Practice for Minimizing Dosimetry Errors in Radiation Hardness Testing of Silicon Electronic Devices Using Co-60 Sources. Jun 2005.

[31] D. Dudáš. Personal communications.

[32] E. Verbitskaya Z. Li, C. J. Li. Study of Bulk Damage in High Resistivity Silicon Detectors Irradiated by High Dose of Cobalt-60 gamma irradiation. *IEEE Transactions on Nuclear Science*, Vol. 44 No. 3, Jun 1997.

[33] M. Mikeštíková et al. Evaluation of Bulk and Surface Radiation Damage of Silicon Sensors for the ATLAS Upgrade. *PoS(Vertex 2014)050*, 2014.

List of Figures

List of Tables